Sensitivity of quantum gate fidelity to laser phase and intensity noise

X. Jiang,[1] J. Scott,[1] M. Friesen,[1] and M. Saffman[1,2]

[1]*Department of Physics, University of Wisconsin-Madison, 1150 University Avenue, Madison, WI 53706*

[2]*ColdQuanta, Inc., Madison, WI 53703*

(Dated: September 19, 2022)

The fidelity of gate operations on neutral atom qubits is often limited by fluctuations of the laser drive. Here, we quantify the sensitivity of quantum gate fidelities to laser phase and intensity noise. We first develop models to identify features observed in self-heterodyne noise spectra, focusing on the effects of white noise and servo bumps. In the weak-noise regime, characteristic of well-stabilized lasers, we show that an analytical theory based on perturbative solution of a master equation agrees very well with numerical simulations that incorporate phase noise. We compute quantum gate fidelities for one- and two-photon Rabi oscillations and show that they can be enhanced by an appropriate choice of Rabi frequency. We also analyze the influence of intensity noise with spectral support smaller than the Rabi frequency. Our results establish requirements on laser noise levels needed to achieve desired gate fidelities.

I. INTRODUCTION

Logical gate operations on matter qubits rely on coherent driving with electromagnetic fields. For solid state qubits these are generally at microwave frequencies of 1-10 GHz. For atomic qubits microwave as well as optical fields with carrier frequencies of several hundred THz are used for gates. High fidelity gate operations require well controlled fields with very low phase and amplitude noise. In this paper we quantify the influence of control field noise on the fidelity of gate operations on qubits. While we mainly focus on the case of optical control with lasers, our results are also applicable to high fidelity control of solid state qubits with microwave frequency fields.

Since the limits imposed on qubit coherence and gate fidelity by control field noise are of central importance in the quest for improving performance, the topic has been treated in a number of earlier works. Relaxation of qubits in the presence of noise, with and without a driving field was analyzed in [1–8]. Using a filter function methodology the influence of control field noise on gate fidelity was analyzed in a series of papers by Biercuk and collaborators[9–12]. In Ref. [11] experimental measurements based on adding noise to microwave control signals were compared with the theoretical results. Subsequent work[13–15] has concentrated on qubit control with optical frequency fields, including the application to Rydberg gates for neutral atom qubits[13]. While it was shown convincingly in [16] that filtering of the laser phase noise spectrum improves the fidelity of coherent Rydberg atom excitation, a quantitative theory of the influence of laser noise on qubit control that includes the widely used approach of two-photon excitation is not available in the existing literature.

We develop here a detailed theory of the dependence of gate fidelity on the noise spectrum of the driving field based on a perturbative solution of the master equation. Results for the cases of one- and two-photon driving are presented as well as average control fidelities together with the fidelity achieved when the qubit starts in a computational basis state, which is of particular relevance to Rydberg excitation experiments. We show that the spectral distribution of phase and amplitude noise relative to the Rabi frequency of the qubit drive is an important parameter that determines the extent to which noise impacts gate fidelity. When the noise spectrum is peaked near the Rabi frequency the deleterious effects are most prominent. Our one-photon, state-averaged results for the influence of the noise spectrum on gate error are similar to, yet different from the predictions of filter function theory[10]. The differences are detailed in Appendix A and can be traced to the use of different gate fidelity measures here, and in[10].

We proceed in Sec. II with a summary of the theory of the laser lineshape and its' relation to self-heterodyne spectral measurements. In Sec. III we show how the theory can be used to extract parameters describing the laser phase noise spectrum from experimental self-heterodyne measurements. In Sec. IV we present a master equation description for the coherence of Rabi oscillations with a noisy drive field. A Schrödinger equation based numerical simulation is given in Sec. V, followed by a quasi-static approximation in Sec. VI. The effect of intensity noise on gate fidelity is presented in Sec. VII. The results obtained, as well as a comparison with filter function theory, are summarized in Sec. VIII.

II. LASER NOISE ANALYSIS

The self-heterodyne interferometer is a powerful tool for characterizing laser noise [17]. In a typical arrangement, the heterodyne circuit outputs a current $I(t)$ (or normalized current $i(t)$, as defined below) containing the noise signal. The resulting power spectral density, $S_i(f)$, provides a convenient proxy for laser field and frequency fluctuations, $S_E(f)$ and $S_{\delta\nu}(f)$, although the correspondence is not one-to-one. In this section, we derive these three functions and show how they are related, focusing on the regime of weak frequency noise. While many of the results in this section have been obtained previously,

we re-derive them here to establish a common framework and notation. We then apply our results to two types of noise affecting atomic qubit experiments: white noise and servo bumps. This analysis forms the starting point for the master equation calculations that follow.

The Rabi oscillations of a qubit are driven by a classical laser field, which we define as

$$\mathbf{E}(t) = \frac{\hat{\mathbf{e}} E_0(t)}{2} e^{-i[2\pi\nu t + \phi(t)]} + \text{c.c.},\tag{1}$$

where c.c. stands for complex conjugate. Here we assume the polarization vector $\hat{\mathbf{e}}$ and E_0 may be complex. Fluctuations of the laser field are a significant source of decoherence in current atomic qubit experiments, and are the focus of the present work. The fluctuations may occur in any of the field parameters, $\hat{\mathbf{e}}$, E_0, or ϕ, where the latter is the phase of the drive. For lasers of interest, the fluctuations predominantly occur in the phase and amplitude variables. In this work, we therefore ignore noise in the polarization vector and focus on the fluctuations of $\phi(t)$. The effect of relative intensity noise (RIN), where the intensity is proportional to $|E_0(t)|^2$ is considered briefly in Sec. VII.

Phase fluctuations may alternatively be analyzed in terms of fluctuations of the frequency, $\nu(t) = \nu_0 + \delta\nu(t)$, which are related to phase fluctuations through the relation

$$\phi(t) = \int_{t_0}^{t_0+t} 2\pi\delta\nu(t')dt',\tag{2}$$

where t_0 is a reference time. The fluctuations of $\delta\nu(t)$ [or $\phi(t)$] have a direct influence on the Rabi oscillations, and must therefore be carefully characterized. A compact description of a general fluctuating variable $X(t)$ is given by its autocorrelation function. Making use of the ergodic theorem, we can equate ensemble and time averages to obtain the following definition for the autocorrelation function:

$$R_X(\tau) = \langle X(t)X^*(t+\tau)\rangle$$
$$\equiv \lim_{T\to\infty} \frac{1}{2T} \int_{-T}^{T} X(t)X^*(t+\tau)dt.\tag{3}$$

Throughout this work, we will only consider random variables, $X(t)$, that are wide-sense stationary.

According to the Wiener-Khintchine theorem, the autocorrelation function of $X(t)$ is related to its noise power spectrum by the Fourier transform,

$$S_X(f) = \int_{-\infty}^{\infty} R_X(\tau)e^{-i2\pi f\tau}d\tau,\tag{4}$$

and its inverse transform,

$$R_X(\tau) = \int_{-\infty}^{\infty} S_X(f)e^{i2\pi f\tau}df,\tag{5}$$

where in this work, we only consider two-sided power spectra.

The main goal of this work is to characterize the noise spectrum of $E(t)$. However, $S_E(f)$ (also called the laser lineshape) cannot be measured directly, due to the high frequency of the carrier. We must therefore transduce the power spectrum to lower frequencies. Here, we consider the self-heterodyne transduction technique, in which the laser field is split, delayed, and recombined to perform interferometric measurements. The resulting signal is read out as a photocurrent containing a direct imprint of the underlying noise spectrum. For the dimensionless photocurrent $i(t)$, which we define below, the self-heterodyne power spectrum is denoted $S_i(f)$.

In this section, we derive the interrelated power spectra of $S_E(f)$ and $S_i(f)$, which are in turn functions of the underlying noise spectrum $S_{\delta\nu}(f)$ [or $S_\phi(f)$]. To perform noisy gate simulations, as discussed in later sections, one would like to use actual self-heterodyne experimental data to characterize the underlying noise spectra. In principle, such a deconvolution cannot be implemented exactly [18]. However, we will show that reliable results for the noise power may indeed be obtained, particularly for lasers with very low noise levels, such as the locked and filtered lasers used in recent qubit experiments.

A. Laser Lineshape

The autocorrelation function for the laser field is defined as [18, 19]

$$R_E(\tau) = \langle E(t)E(t+\tau)\rangle,\tag{6}$$

where we note that $E(t)$ is the real, scalar amplitude of $\mathbf{E}(t)$. This function contains information about both the carrier signal, centered at frequency ν_0, and the fluctuations, which are typically observed as a fundamental broadening of the carrier peak. Additional features of importance for qubit experiments include structures away from the peak that may be caused by the laser locking and filtering circuitry, such as the "servo bump", discussed in detail below.

The time average in Eq. (6) has been evaluated by a number of authors. For completeness, we summarize these derivations here, following the approach of Ref. [19]. Let us begin by assuming the noise process is strongly stationary, so that Eq. (6) does not depend on t; for simplicity, we set $t = 0$. Using Eqs. (1) and (6) and trigonometric identities, defining $E_0 = |E_0|e^{-i\alpha}$, and neglecting fluctuations of E_0, we then have

$$\begin{aligned}R_E(\tau) = \frac{|E_0|^2}{2}\Big\{ &\cos(2\pi\nu_0\tau)\langle\cos[\phi(\tau)-\phi(0)]\rangle \\ &+ \cos(2\pi\nu_0\tau)\langle\cos[\phi(\tau)+\phi(0)+2\alpha]\rangle \\ &- \sin(2\pi\nu_0\tau)\langle\sin[\phi(\tau)-\phi(0)]\rangle \\ &- \sin(2\pi\nu_0\tau)\langle\sin[\phi(\tau)+\phi(0)+2\alpha]\rangle\Big\}.\end{aligned}\tag{7}$$

We then assume the phase difference $\Phi(\tau) \equiv \phi(\tau) - \phi(0)$ to be a Gaussian random variable centered at $\Phi(\tau) = 0$,

with probability distribution

$$p(\Phi) = \frac{1}{\sigma_\Phi \sqrt{2\pi}} e^{-\Phi^2/2\sigma_\Phi^2},$$

and variance $\overline{\Phi^2} = \sigma_\Phi^2$. Here, the bar denotes an ensemble average. According to the ergodic theorem, ensemble and time averages should give the same result, so that

$$\sigma_\Phi^2(\tau) = \langle [\phi(\tau) - \phi(0)]^2 \rangle = 2R_\phi(0) - 2R_\phi(\tau), \quad (8)$$

where we note that

$$\langle \phi^2(0) \rangle = \langle \phi^2(\tau) \rangle = R_\phi(0).$$

Again, making use of the ergodic theorem, we have

$$\langle \cos(\Phi) \rangle = e^{-\sigma_\Phi^2/2} \quad \text{and} \quad \langle \sin(\Phi) \rangle = 0, \quad (9)$$

which is also known as the moment theorem for Gaussian random variables. Finally we note that only biased

variables like $\phi(\tau) - \phi(0)$ are Gaussian. An unbiased variable like $\phi(\tau) + \phi(0)$ is simply a random phase, for which $\langle \cos[\phi(\tau) + \phi(0)] \rangle = \langle \sin[\phi(\tau) + \phi(0)] \rangle = 0$. Combining these facts, we obtain the important relation [20]

$$R_E(\tau) = \frac{|E_0|^2}{2} \cos(2\pi\nu_0\tau) e^{[R_\phi(\tau) - R_\phi(0)]}. \quad (10)$$

Note that since ϕ can take any value, $R_\phi(0)$ does not have physical significance on its own; only the difference $R_\phi(\tau) - R_\phi(0)$ is meaningful.

Another useful form for Eq. (10) can be obtained from the relation $2\pi\delta\nu(t) = \partial\phi/\partial t$, together with Eq. (4) and the stationarity of $R_\phi(t)$, yielding

$$S_{\delta\nu}(f) = f^2 S_\phi(f). \quad (11)$$

Applying trigonometric identities, we then obtain the following, well-known results for the laser lineshape [18]:

$$R_E(\tau) = \frac{|E_0|^2}{2} \cos(2\pi\nu_0\tau) \exp\left[-2 \int_{-\infty}^{\infty} S_{\delta\nu}(f) \frac{\sin^2(\pi f \tau)}{f^2} \, df \right], \quad (12)$$

and

$$S_E(f) = \frac{|E_0|^2}{2} \int_{-\infty}^{\infty} \cos(2\pi f \tau) \cos(2\pi\nu_0\tau) \exp\left[-2 \int_{-\infty}^{\infty} S_{\delta\nu}(f') \frac{\sin^2(\pi f' \tau)}{(f')^2} \, df' \right] d\tau. \quad (13)$$

It is common to adopt a lineshape that is centered at zero frequency; henceforth, we therefore set $\nu_0 = 0$. We note that $S_E(f)$ is properly normalized here, with $\int_{-\infty}^{\infty} S_E(f) df = |E_0|^2/2$. Thus, fluctuations that broaden the lineshape also reduce the peak height.

Some additional interesting results follow from Eq. (13). First, in the absence of noise [$S_{\delta\nu} = 0$], we see that the laser lineshape immediately reduces to an unbroadened carrier signal: $S_E(f) = (|E_0|^2/2)\delta(f)$. Second, when $S_{\delta\nu}$ is nonzero but small, as is typical for a locked and filtered laser, the exponential term in Eq. (13) may be expanded to first order, yielding [21]

$$2S_E(f)/|E_0|^2 \approx [1 - R_\phi(0)]\delta(f) + S_\phi(f). \quad (14)$$

This approximation is generally very good, but breaks down in the asymptotic limit $\tau \to \infty$ of the τ integral, and therefore the limit $f \to 0$. To see this, we note that $\sin^2(\pi f \tau)$ may be replaced by its average value of $1/2$ in the integral; for nonvanishing values of $S_{\delta\nu}(0)$, the argument of the exponential then diverges. To estimate the frequency f_x, below which Eq. (14) breaks down, we set the argument of the exponential in Eq. (14) to $1/2$:

$$2 \int_{f_x}^{\infty} \frac{S_{\delta\nu}(f)}{f^2} df \approx \frac{1}{2}. \quad (15)$$

This criterion clearly depends on the noise spectrum.

To conclude, we note that for some analytical calculations (such as the servo-bump analysis, described below), it may be convenient or pedagogical to separate the noise spectrum into distinct components: $S_{\delta\nu}(f) = S_{\delta\nu,1}(f) + S_{\delta\nu,2}(f)$, corresponding to different physical noise mechanisms. From Eq. (12), the resulting lineshapes can then be written as

$$R_E(\tau) = \frac{2}{|E_0|^2} R_{E,1}(\tau) R_{E,2}(\tau), \quad (16)$$

where $R_{E,1}(\tau)$ and $R_{E,2}(\tau)$ are the autocorrelation functions corresponding to $S_{\delta\nu,1}(f)$ and $S_{\delta\nu,2}(f)$. Applying the Fourier convolution theorem, we obtain

$$S_E(f) = 2|E_0|^{-2} \int_{-\infty}^{\infty} S_{E,1}(f - f') S_{E,2}(f') df'. \quad (17)$$

B. Self-Heterodyne Spectrum

We consider the self-heterodyne optical circuit shown in Fig. 1. As depicted in the diagram, one of the paths is delayed by time t_d, through a long optical fiber, and then
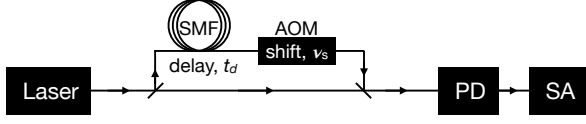
FIG. 1. Self-heterodyne setup. The laser signal is split equally between two paths. One path passes through a single-mode fiber (SMF), where it is delayed by time t_d. It then passes through an acousto-optic modulator (AOM), where its frequency is shifted by ν_s. The interfering signals are combined and measured by a photodiode (PD), and finally processed through a spectrum analyzer (SA).

shifted in frequency by ν_s, by means of an acousto-optic modulator. Here, the delay loop allows us to interfere phases at different times, while the frequency shift provides a beat tone that is readily accessible to electronic measurements, since it occurs at submicrowave frequencies, $\nu_s \approx 100$ MHz. The two beams are then recombined and the total intensity is measured by a photodiode, using conventional measurement techniques.

For simplicity, we assume the laser signal is split equally between the two paths, although unequal splittings may also be of interest [22]. The recombined field amplitude is defined as

$$
\begin{aligned}
E(t) = \frac{|E_0|}{2} \Big\{ &\exp[-i2\pi\nu_0 t - i\phi(t) - i\alpha] \\
&+ \exp[-i2\pi(\nu_0 + \nu_s)(t - t_d) - i\phi(t - t_d) - i\alpha] \Big\} + \text{c.c.}
\end{aligned}
$$
(18)

The output current of the photodiode is then proportional to $|E(t)|^2$. For convenience, we consider instead a dimensionless photocurrent $i(t)$ given by

$$
\begin{aligned}
i(t) = \frac{1}{2} \Big\{ &\cos\left[2\pi\nu_0 t + \phi(t) + \alpha\right] \\
&+ \cos\left[2\pi(\nu_0 + \nu_s)(t - t_d) + \phi(t - t_d) + \alpha\right] \Big\}^2.
\end{aligned}
$$
(19)

The corresponding autocorrelation function is defined as

$$
R_i(\tau) = \langle i(t)i(t + \tau)\rangle. \tag{20}
$$

The evaluation of $R_i(\tau)$ is greatly simplified by noting that cosine terms with ν_0 in their argument average to zero in a physically realistic measurement. Again making use of the fact that unbiased variables like $\phi(\tau) + \phi(0)$ are random phases (i.e., nongaussian), we find that

$$
\begin{aligned}
R_i(\tau) = 4 \\
+ 2\langle\cos[2\pi\nu_s\tau + \phi(t) - \phi(t - t_d) - \phi(t + \tau) + \phi(t + \tau - t_d)]\rangle.
\end{aligned}
$$
(21)

Taking the same approach as in the derivation of $R_E(\tau)$, we take $\Phi' = \phi(t) - \phi(t - t_d) - \phi(t + \tau) + \phi(t + \tau - t_d)$

to be a Gaussian random variable centered at zero, and apply the Gaussian moment relations,

$$
\langle\cos(\Phi')\rangle = e^{-\sigma_{\Phi'}^2/2} \quad \text{and} \quad \langle\sin(\Phi')\rangle = 0, \tag{22}
$$

where

$$
\sigma_{\Phi'}^2 = \langle[\phi(t) - \phi(t - t_d) - \phi(t + \tau) + \phi(t + \tau - t_d)]^2\rangle. \tag{23}
$$

In this way we obtain

$$
\begin{aligned}
R_i(\tau) = 4 + 2\cos(2\pi\nu_s\tau) \\
\times \exp[2R_\phi(\tau) + 2R_\phi(t_d) - 2R_\phi(0) \\
- R_\phi(\tau - t_d) - R_\phi(\tau + t_d)].
\end{aligned}
$$
(24)

Here, the cosine function represents the beat tone, and the noise information is reflected in its amplitude. It can be seen that the corresponding power spectrum, $S_i(f)$, includes a central peak, $\delta(f)$, which contains no information about the laser noise, and two broadened but identical satellite peaks, centered at $f = \pm\nu_s$. We now recenter $R_i(\tau)$ at one of the satellite peaks, as consistent with typical self-heterodyne measurements, such that

$$
\begin{aligned}
R_i(\tau) \to R_i(\tau) = \exp[2R_\phi(\tau) + 2R_\phi(t_d) - 2R_\phi(0) \\
- R_\phi(\tau - t_d) - R_\phi(\tau + t_d)].
\end{aligned}
$$
(25)

Applying trigonometric identities, we then obtain

$$
R_i(\tau) = \exp\left[-8\int_{-\infty}^{\infty} S_{\delta\nu}(f)\frac{\sin^2(\pi f\tau)\sin^2(\pi f t_d)}{f^2}df\right].
$$
(26)

Taking $S_{\delta\nu}(f)$ to be an even function, we can write

$$
S_i(f) = \int_{-\infty}^{\infty} \cos(2\pi f\tau)R_i(\tau)d\tau. \tag{27}
$$

We note that the self-heterodyne peak defined in this way is normalized such that $\int_{-\infty}^{\infty} S_i(f)df = R_i(0) = 1$.

In the absence of noise $[S_{\delta\nu} = 0]$, we see from Eqs. (26) and (27) that the self-heterodyne power spectrum reduces to the bare carrier: $S_i(f) = \delta(f)$. For nonzero but small $S_{\delta\nu}$, we can expand the exponential in Eq. (26), as was done in Eq. (14), to obtain

$$
\begin{aligned}
S_i(f) \approx \big[1 + 2R_\phi(t_d) - 2R_\phi(0)\big]\delta(f) \\
+ 4\sin^2(\pi f t_d)S_\phi(f).
\end{aligned}
$$
(28)

The second term in this expression is closely related to the envelope-ratio power spectral density described in Ref. [23], following on the earlier work of Ref. [24], and provides a theoretical basis for the former.

As in the derivation of Eq. (14), the expansion leading to Eq. (28) breaks down at low frequencies. However, the well-known "scallop" features in the power spectrum are seen to arise from the factor $\sin^2(\pi f t_d)$. This result clarifies the relation between the self-heterodyne signal,
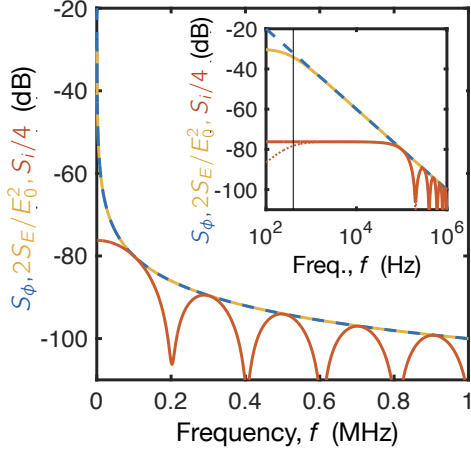
FIG. 2. White-noise power spectral densities, $S_\phi(f)$ (blue), $2S_E(f)/E_0^2$ (gold), and $S_i(f)/4$ (red), defined in Eqs. (32), (35), and (38), respectively, for noise strength $h_0 = 100$ Hz^2/Hz. Here we have omitted the δ-function peak in $S_i(f)$. The inset shows the same quantities plotted on a logarithmic frequency scale. An approximate form for $S_i/4$ (red, dotted) is obtained from Eq. (29). The cutoff f_x (vertical black), defined in Eq. (15), indicates the frequency where Eq. (14) begins to fail.

the underlying laser noise, and the laser lineshape. The latter relation is given by

$$|E_0|^2 S_i(f) \approx 2\sin^2(\pi f t_d) S_E(f), \tag{29}$$

where we have omitted the central carrier peak.

To conclude, we again consider the possibility that the noise spectrum may be separated into distinct components, $S_{\delta\nu}(f) = S_{\delta\nu,1}(f) + S_{\delta\nu,2}(f)$. As for the laser lineshape, the self-heterdyne autocorrelation function may then be written as

$$R_i(\tau) = R_{i,1}(\tau)R_{i,2}(\tau), \tag{30}$$

yielding the combined power spectrum

$$S_i(f) = \int_{-\infty}^{\infty} S_{i,1}(f-f')S_{i,2}(f')df'. \tag{31}$$

C. White Noise

The self-heterodyne laser noise measurements, reported below, are well described by a combination of white noise and a Gaussian servo bump. We now obtain analytical results for the $S_E(f)$ and $S_i(f)$ power spectra, for these two noise models. The results for white noise are well-known [25]. However we reproduce them here for completeness.

The underlying noise spectrum for white noise is given by

$$S_{\delta\nu} = h_0 \qquad \text{or} \qquad S_\phi(f) = \frac{h_0}{f^2} \tag{32}$$

where h_0 is the amplitude of the power spectral density of the frequency noise and has units of Hz^2/Hz.

Note that it is common to use a one-sided noise spectrum for such calculations; however we use a two-sided spectrum here. Our results may therefore differ by a factor of 2 from others reported in the literature. The most straightforward calculation of $R_\phi(\tau)$, from Eq. (5), immediately encounters a singularity. We therefore proceed by calculating $R_E(\tau)$ from Eq. (12). Setting $\nu_0 = 0$, to center the power spectrum, then gives

$$R_E(\tau) = \frac{|E_0|^2}{2}e^{-2\pi^2 h_0|\tau|}. \tag{33}$$

From Eq. (10), we can identify

$$R_\phi(\tau) - R_\phi(0) = -2\pi^2 h_0|\tau|, \tag{34}$$

where the singularity has now been absorbed into $R_\phi(0)$. Solving for the laser lineshape yields

$$S_E(f) = \frac{|E_0|^2}{2}\frac{h_0}{f^2 + (\pi h_0)^2}, \tag{35}$$

for which the full-width-at-half-maximum (FWHM) linewidth is $2\pi h_0$. Away from the carrier peak, which is very narrow for a locked and well-filtered laser, we find

$$2S_E(f)/E_0^2 \approx \frac{h_0}{f^2} = S_\phi(f), \tag{36}$$

which is consistent with Eq. (14).

We can also evaluate the self-heterodyne autocorrelation function, Eq. (25), obtaining

$$R_i(\tau) = \exp\left[-2\pi^2 h_0(2t_d + 2|\tau| - |\tau - t_d| - |\tau + t_d|\right], \tag{37}$$

and the corresponding power spectrum,

$$S_i(f) = \frac{2h_0}{f^2 + (2\pi h_0)^2} + e^{-4\pi^2 h_0 t_d}\bigg\{\delta(f) \tag{38}$$

$$-\frac{2h_0}{f^2 + (2\pi h_0)^2}\left[\cos(2\pi f t_d) + \frac{2\pi h_0}{f}\sin(2\pi f t_d)\right]\bigg\}.$$

It is interesting to visualize the results and approximations employed above. In Fig. 2 we plot the white-noise power spectral densities $S_\phi(f)$, $S_E(f)$, and $S_i(f)$ corresponding to Eqs. (32), (35)], and (38), on both linear and logarithmic scales, for the noise amplitude $h_0 = 100$ Hz^2/Hz. In the inset, we also plot the approximate relation between $S_i(f)$ and $S_E(f)$ given by Eq. (29), which clarifies how self-heterodyne measurements may be used to characterize the laser noise. Here, we also plot the crossover frequency f_x from Eq. (15), below which the approximations in Eq. (29) begin to fail. For the case of white noise, this expression can be evaluated analytically, giving $f_x = 4h_0$.

The scallop features in Fig. 2 are caused by beating between the interfering fields in the self-heterodyne circuit. We note that, in principle, the fine-scale noise features present in $S_\phi(f)$ or $S_E(f)$ are inherited by $S_i(f)$. However some features are obscured by the scallops, which suppress the measured signal at frequency intervals of $\Delta f = 1/t_d$.

D. Servo Bump

Lasers are commonly stabilized by locking to narrow-linewidth reference cavities[26]. The error signal derived from the reference cavity is fed into a feedback system or servo loop [21], and the finite bandwidth of the servo loop induces peaks in $S_{\delta\nu}(f)$ called servo bumps, which are typically shifted above and below the central peak by frequencies on the order of 1 MHz. We find that experimental servo bumps have approximately Gaussian shapes. In fact, we find that the full noise model is well described by a Gaussian servo bump combined with white noise, as defined by

$$
\begin{aligned}
S_{\delta\nu}(f) &= h_0 + h_g \exp\left[-\frac{(f-f_g)^2}{2\sigma_g^2}\right] + h_g \exp\left[-\frac{(f+f_g)^2}{2\sigma_g^2}\right] \\
&= h_0 + \frac{s_g f_g^2}{\sqrt{8\pi}\sigma_g} \exp\left[-\frac{(f-f_g)^2}{2\sigma_g^2}\right] + \frac{s_g f_g^2}{\sqrt{8\pi}\sigma_g} \exp\left[-\frac{(f+f_g)^2}{2\sigma_g^2}\right].
\end{aligned} \tag{39}
$$

Here, h_g is the bump's height, σ_g is its width, with a FWHM given by $\sqrt{\ln 4}\,\sigma_g$, and f_g is the center frequency of the bump.

In the second line of Eq. (39), we use an alternative expression for the bump height, in terms of its total, dimensionless phase-noise power, $s_g = \int_{-\infty}^{\infty} S_{\phi,g}(f)df$, where the subscript g refers to the Gaussian noise components. We use this expression in the simulations described below, to explore the effects of different bump shapes. To perform the s_g conversion here, we note that $S_{\phi,g}(f)$ is actually singular at $f = 0$, causing its integral to diverge. We can regularize this divergence by assuming that the servo bump is narrow (which appears to be true in many experiments), and by making the substitution

$$
S_\phi(f) = S_{\delta\nu}(f)/f^2 \approx S_{\delta\nu}(f)/f_g^2, \tag{40}
$$

yielding

$$
s_g \approx \sqrt{8\pi}\sigma_g h_g/f_g^2, \tag{41}
$$

which is the form used in Eq. (39). We can think of this expression as describing the noise power in just the servo bump, and not the low-frequency portion of the spectrum. We emphasize that the latter is not ignored but it is subsumed into the white noise, which we treat separately.

We first consider just the Gaussian term in Eq. (39), setting $h_0 = 0$. Fourier transforming Eq. (40), we obtain

$$
R_\phi(\tau) \approx s_g \cos(2\pi f_g\tau)e^{-2\pi^2\sigma_g^2\tau^2}. \tag{42}
$$

Thus for $s_g \ll 1$, Eq. (14) gives

$$
\begin{aligned}
2S_E(f)/|E_0|^2 \approx \delta(f) &+ \frac{h_g}{f_g^2}\exp\left[-\frac{(f-f_g)^2}{2\sigma_g^2}\right] \\
&+ \frac{h_g}{f_g^2}\exp\left[-\frac{(f+f_g)^2}{2\sigma_g^2}\right],
\end{aligned} \tag{43}
$$

and Eq. (28) gives

$$
\begin{aligned}
S_i(f) \approx \delta(f) &+ \frac{4h_g}{f_g^2}\sin^2(\pi f t_d)\exp\left[-\frac{(f-f_g)^2}{2\sigma_g^2}\right] \\
&+ \frac{4h_g}{f_g^2}\sin^2(\pi f t_d)\exp\left[-\frac{(f+f_g)^2}{2\sigma_g^2}\right].
\end{aligned} \tag{44}
$$

The white noise component of $S_{\delta\nu}(f)$ can now be included, and using Eqs. (17) and (31), yields

$$
S_E(f) = \frac{2}{|E_0|^2}\int_{-\infty}^{\infty} S_{E,w}(f-f')S_{E,g}(f')df', \tag{45}
$$

$$
S_i(f) = \int_{-\infty}^{\infty} S_{i,w}(f-f')S_{i,g}(f')df', \tag{46}
$$

where the subscripts w and g refer to white and Gaussian power spectra, which have already been computed. We solve these integrals, approximately, by noting that a convolution between two peaks, with very different widths, is dominated by the wider peak. We further note that, for the lasers of interest here, the servo bump is much wider than the white-noise Lorentzian peak, which is in turn much wider than a delta function. Hence, we find that

$$
\begin{aligned}
2S_E(f)/E_0^2 \approx &\frac{h_0}{f^2+(\pi h_0)^2} + \frac{h_g}{f_g^2}\exp\left[-\frac{(f-f_g)^2}{2\sigma_g^2}\right] \\
&+ \frac{h_g}{f_g^2}\exp\left[-\frac{(f+f_g)^2}{2\sigma_g^2}\right],
\end{aligned} \tag{47}
$$

and

$$
\begin{aligned}
S_i(f) \approx &\frac{2h_0}{f^2+(2\pi h_0)^2} + e^{-4\pi^2 h_0 t_d}\Bigg\{\delta(f) \\
&- \frac{2h_0}{f^2+(2\pi h_0)^2}\left[\cos(2\pi f t_d) + \frac{2\pi h_0}{f}\sin(2\pi f t_d)\right]\Bigg\} \\
&+ \frac{4h_g}{f_g^2}\sin^2(\pi f t_d)\exp\left[-\frac{(f-f_g)^2}{2\sigma_g^2}\right] \\
&+ \frac{4h_g}{f_g^2}\sin^2(\pi f t_d)\exp\left[-\frac{(f+f_g)^2}{2\sigma_g^2}\right].
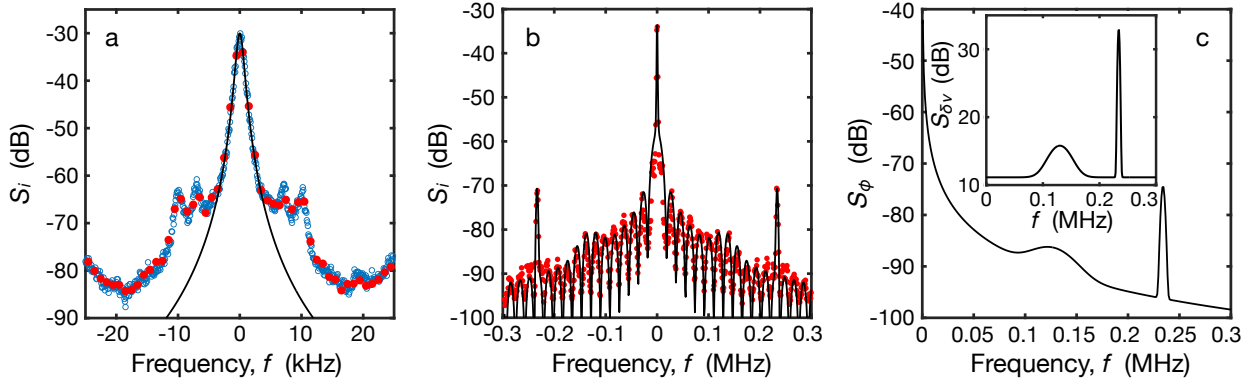\end{aligned} \tag{48}
$$

FIG. 3. Self-heterodyne data from a 1040 nm solid-state Ti:Sa laser (MSquared SolsTiS) with fits to noise models. The laser was locked to a reference cavity with linewidth of approximately 5 kHz using the Pound-Drever-Hall method[26]. (a) Self-heterodyne power spectral density, obtained in a 50 kHz frequency window with RBW = 100 Hz (open blue circles) and in a 600 kHz window with RBW = 300 Hz (closed red markers). An optical delay fiber of 11 km is used for both data sets, corresponding to a delay time of $t_d = 5.445 \times 10^{-5}$ s. The data are shifted horizontally to center their peaks at zero frequency, and the peak data are then fit to Eq. (49) (black line), obtaining $\alpha = 5/2$ and $\sigma = 240$ Hz. The data are finally renormalized (i.e., shifted vertically) to ensure the correct total power, as described in the main text. (b) Same red data set as (a), plotted over a wider frequency window. The data are fit to Eq. (48), including white noise and two Gaussian servo bumps, obtaining $h_0 = 13$ Hz^2/Hz, $h_{g1} = 25$ Hz^2/Hz, $\sigma_{g1} = 18$ kHz, $f_{g1} = 130$ kHz, and $h_{g2} = 2.0 \times 10^3$ Hz^2/Hz, $\sigma_{g12} = 1.5$ kHz, $f_{g2} = 234$ kHz. (c) Phase and frequency power spectral densities, $S_\phi(f)$ and $S_{\delta\nu}(f)$ (inset), resulting from the fitting.

In the following section, we apply these equations as fitting forms for experimental self-heterodyne data.

III. LASER CHARACTERIZATION

To help visualize these results, we now characterize a stabilized solid-state Ti:Sa laser used in quantum gate experiments with atomic qubits[27]. In Fig. 3(a), we plot two experimental data sets from the same laser (red and blue markers). We find that the central peak is broadened more significantly than the resolution bandwidth (RBW) settings of the spectrum analyzer. The corresponding linewidths are approximately equal, despite their different RBW, suggesting that RBW is not the only source of broadening.

Although the central peak does not exhibit a clear characteristic form, we find that that it is well described by

$$S_{i,\text{peak}}(f) = \frac{s_p \sigma^{2\alpha-1}}{(f^2 + \pi^2\sigma^2)^\alpha}. \qquad (49)$$

Fitting the data to this form yields $\alpha = 5/2$ and $\sigma = 240$ Hz. The corresponding FWHM is 850 Hz, which is indeed several times larger than the RBW of the measurements. Integrating Eq. (49) over frequency yields $4s_p/3\pi^4$. The data are therefore shifted vertically in Fig. 3(a) to give the correct normalization, $\int_{-\infty}^{\infty} S_i(f)df = 1$.

After this normalization step, the self-heterodyne data away from the peak are fit to Eq. (48), where we introduce two distinct servo bumps, obtaining the result shown in Fig. 3(b) (black line). The corresponding power

spectral densities for the noise are plotted in Fig. 3(c). We can use these results to determine the fractional noise power in different components of the S_ϕ spectrum For the first servo bump, we obtain the fractional power $s_{g1} = 0.00027$, and for the second servo bump, we obtain the fractional power $s_{g2} = 0.00013$. Together, these represent a small but non-negligible fraction of the total laser power.

The spectral features of the locked laser can be related to the stabilization system. The laser is stabilized using three feedback loops: a slow piezo with bandwidth of approximately 50 Hz, a faster piezo with bw of 100 kHz, and an electro-optic phase modulator with bandwidth of several MHz. The servo bumps centered at f_{g1} and f_{g2} are attributable to the fast piezo and the electro-optic modulator.

IV. DENSITY MATRIX SOLUTIONS FOR RABI OSCILLATIONS

In this section, we compute the density matrix of a qubit undergoing Rabi oscillations driven by a laser with frequency noise. The calculation involves taking an average over all possible noise realizations. In Sec. IV A, we perform a Fourier expansion of a generic Gaussian noise process, which is incorporated into the master equation calculation of Sec. IV B, and is used again in the numerical simulations of Sec. V. In Sections IV C and IV D, we use our master equation results to compute one and two-photon gate fidelities for the Rabi oscillations.

A. Time-Series Expansion of the Laser Noise

A real, fluctuating Gaussian process $X(t)$, with zero mean and variance σ_X^2, can generally be expressed as a Fourier time series:

$$X(t) = \sum_{j=1}^{\infty} x_j \cos(2\pi f_j t + \varphi_j), \qquad (50)$$

where $f_j = j\Delta f$. Here, we have defined $X(0) = 0$ for convenience. The random variables x_j can be selected as Rayleigh-distributed random values [28], while the random variables φ_j are uniformly distributed over $[0, 2\pi]$.

We can compute the variance of $X(t)$ as

$$\sigma_X^2 = \left\langle \sum_{j,k} x_j x_k \cos(2\pi f_j t + \varphi_j) \cos(2\pi f_k t + \varphi_k) \right\rangle, \qquad (51)$$

where an average is taken over the various random variables. Since these variables are assumed to be statistically independent, the double sum vanishes, except for the case $j = k$. Hence,

$$\sigma_X^2 = \sum_{j=1}^{\infty} \langle x_j^2 \rangle / 2. \qquad (52)$$

The variance is also related to the same-time autocorrelation function, defined in Eq. (3), such that

$$\sigma_X^2 = R_X(0) = 2 \int_0^{\infty} S_X(f) df = 2 \sum_{j=1}^{\infty} S_{X,j} \Delta f, \qquad (53)$$

where we have assumed that $S_x(f)$ is an even function, and converted the integral to a series representation, with $S_{X,j} = S_X(f_j)$.

Comparing Eqs. (52) and (53), we note the correspondence

$$\langle x_j^2 \rangle \leftrightarrow 4 S_{X,j} \Delta f. \qquad (54)$$

To generate time traces of $X(t)$, it is then standard practice to make the following replacement for the random variable x_j in Eq. (50) [28]:

$$x_j \to 2\sqrt{S_{X,j} \Delta f}. \qquad (55)$$

Defined in this way, x_j is deterministic rather than random. The resulting time trace $X(t)$ inherits the correct statistical properties of x_j. Although this procedure cannot account for all random behavior of $X(t)$ [29], it successfully describes most behavior.

The method described above is used to generate random time traces in our numerical simulations, as described below in Sec. V A. These simulations incorporate time traces of the laser phase fluctuations, defined as

$$\phi(t) = \sum_{j=1}^{\infty} 2\sqrt{S_\phi(f_j)\Delta f} \cos(2\pi f_j t + \varphi_j). \qquad (56)$$

Here, we note that, while time-series amplitude coefficients have been replaced by their deterministic averages, the random phases φ_j must still be chosen from the uniform distribution $[0, 2\pi]$. In the following section, we incorporate time traces of the laser frequency fluctuations, defined as

$$\delta\nu(t) = \frac{1}{2\pi}\frac{d\phi}{dt} = \sum_{j=1}^{\infty} \delta\nu_j \sin(2\pi f_j t + \varphi_j), \qquad (57)$$

where

$$\delta\nu_j = -2\sqrt{S_{\delta\nu}(f_j)\Delta f}, \qquad (58)$$

and we make use of the relation $S_{\delta\nu}(f) = f^2 S_\phi(f)$.

B. Time-Series Master Equation

We consider the two-level system $\{|g\rangle, |e\rangle\}$, with corresponding energy levels E_g and E_e, and qubit energy $h\nu_0 = E_e - E_g$. The Hamiltonian for a qubit driven on resonance driven by a monochromatic laser with angular frequency ν_0 and angular Rabi frequency Ω_0, assumed to be real here, is then given by

$$H = \frac{h\nu_0}{2}(|e\rangle\langle e| - |g\rangle\langle g|)$$
$$+ \hbar\Omega_0 \cos(2\pi\nu_0 t)\left[e^{i\phi(t)}|e\rangle\langle g| + e^{-i\phi(t)}|g\rangle\langle e|\right], \qquad (59)$$

where we have explicitly included phase fluctuations $\phi(t)$. Moving to a rotating frame defined by $U(t) = \exp[-i\pi\nu_0 t(|e\rangle\langle e| - |g\rangle\langle g|)]$ and applying a rotating wave approximation (RWA), we obtain the transformed Hamiltonian

$$H' \approx \frac{\hbar\Omega_0}{2}\left[e^{i\phi(t)}|e\rangle\langle g| + e^{-i\phi(t)}|g\rangle\langle e|\right],$$
$$= \frac{\hbar\Omega_0}{2}[\cos\phi(t)\,\sigma_x - \sin\phi(t)\,\sigma_y], \qquad (60)$$

where the Pauli matrices are defined as $\sigma_x = |g\rangle\langle e| + |e\rangle\langle g|$, $\sigma_y = i|g\rangle\langle e| - i|e\rangle\langle g|$, and $\sigma_z = |g\rangle\langle g| - |e\rangle\langle e|$.

In Eqs. (59) and (60), the axis of Rabi rotations shifts with the fluctuating phase $\phi(t)$. Although this description captures the physics of the problem, it is inconvenient for our calculations. We therefore consider a frame that follows the fluctuating phase, in which the rotation axis is fixed [30]. This fluctuating frame is defined by the transformation $U_\varphi(t) = \text{diag}[e^{i\varphi/2}, e^{-i\varphi/2}]$, yielding the Hamiltonian

$$H'' \approx \frac{\hbar\Omega_0}{2}\sigma_x - \frac{\hbar(d\phi/dt)}{2}\sigma_z$$
$$= \frac{\hbar\Omega_0}{2}\sigma_x - \frac{h\delta\nu(t)}{2}\sigma_z$$
$$= \frac{\hbar\Omega_0}{2}\sigma_x - \sum_{j=1}^{\infty}\frac{h\delta\nu_j}{2}\sin(2\pi f_j t + \varphi_j)\sigma_z, \qquad (61)$$

where we make use of Eq. (57), and the only approximation employed is the standard RWA in Eq. (60).

In Eq. (61), we have moved to a frame where Ω_0 now represents the quantizing field, and where $\delta\nu_j$ represents a Rabi driving term, applied simultaneously at multiple frequencies. To formalize this correspondence, we move to the frame where Ω_0 points towards the north pole of the Bloch sphere, as defined by the transformation $U = \exp[-i(\pi/4)\sigma_y]$, obtaining

$$H''' \approx \frac{\hbar\Omega_0}{2}\sigma_z + \sum_{j=1}^{\infty}\frac{h\delta\nu_j}{2}\sin(2\pi f_j t + \varphi_j)\sigma_x. \quad (62)$$

For simplicity, we drop the primed notation on H''' in the following derivations.

We now solve for the time evolution of the density operator, for a two-level system governed by Eq. (62):

$$\hbar\frac{d\rho}{dt} = i[\rho, H]. \quad (63)$$

Although Eq. (62) has the standard form of a Rabi rotation, we note that conventional Rabi techniques are not applicable here, because in the frame of Eq. (62), the initial state of the system is along the driving axis of the Bloch sphere ($\hat{x}$), as discussed below. As such, the time evolution arises entirely from counterrotating terms in Eq. (62), rather than co-rotating terms. (Note that counterrotating and co-rotating refer, here, to the $\delta\nu_j$ fluctuations, not the original Rabi drive.) Moreover, as will become apparent below, it is desirable to consider perturbative corrections to $\rho(t)$, which are of order $\mathcal{O}[\delta\nu_j^2]$ in the frequency fluctuations.

To construct a perturbation theory, we first note that $2\pi\delta\nu_j$ is typically smaller than Ω_0, allowing us to define the dimensionless small parameter, $\delta_j = 2\pi\delta\nu_j/\Omega_0 \lesssim 1$. Defining $\omega_j = 2\pi f_j$, the Hamiltonian becomes

$$\frac{H}{\hbar\Omega_0} = \frac{\sigma_z}{2} + \sum_{j=1}^{\infty}\delta_j\frac{\sigma_x}{2}\sin(\omega_j t + \varphi_j). \quad (64)$$

We can then solve the density matrix by expanding in powers of the small parameter,

$$\rho = \rho_0 + \rho_1 + \rho_2 + \ldots$$
$$= \rho_0 + \sum_{j=1}^{\infty}\delta_j\rho_1^{(j)} + \sum_{j,k=1}^{\infty}\delta_j\delta_k\rho_2^{(j,k)} + \ldots, \quad (65)$$

where $\rho_m^{(j,\ldots)}$ are assumed to be independent of δ_j. Inserting Eqs. (64) and (65) into (63), collecting terms of

equal order in δ_j, and solving up to $\mathcal{O}[\delta_j^2]$ gives

$$\frac{1}{\Omega_0}\frac{d\rho_0}{dt} = i\left[\rho_0, \frac{\sigma_z}{2}\right], \quad (66)$$

$$\sum_{j=1}^{\infty}\frac{\delta_j}{\Omega_0}\frac{d\rho_1^{(j)}}{dt} = \quad (67)$$
$$i\sum_{j=1}^{\infty}\delta_j\left\{\left[\rho_1^{(j)}, \frac{\sigma_z}{2}\right] + \left[\rho_0, \frac{\sigma_x}{2}\sin(\omega_j t + \varphi_j)\right]\right\},$$

$$\sum_{j,k=1}^{\infty}\frac{\delta_j\delta_k}{\Omega_0}\frac{d\rho_2^{(j,k)}}{dt} = \quad (68)$$
$$i\sum_{j,k=1}^{\infty}\delta_j\delta_k\left\{\left[\rho_2^{(j,k)}, \frac{\sigma_z}{2}\right] + \left[\rho_1^{(j)}, \frac{\sigma_x}{2}\sin(\omega_k t + \varphi_k)\right]\right\}.$$

For a Rabi driving experiment, in the frame of Eq. (59), we consider a qubit initialized to the north pole of the Bloch sphere. In the frame of Eq. (64), the corresponding initial state on the Bloch sphere is $\hat{x}$, or $\rho(0) = \frac{1}{2}(1 + \sigma_x)$. Since ρ_0, $\rho_1^{(j)}$, and $\rho_2^{(j,k)}$ are independent of δ_j, the initial conditions for the different terms in the density operator expansion are given by $\rho_0(0) = \frac{1}{2}(1 + \sigma_x)$, with $\rho_1(0) = \rho_2(0) = 0$.

Taking into account the initial conditions, we can solve for each $\rho_1^{(j)}$ separately in Eq. (67), as follows:

$$\frac{1}{\Omega_0}\frac{d\rho_1^{(j)}}{dt} = i\left[\rho_1^{(j)}, \frac{\sigma_z}{2}\right] + i\left[\rho_0, \frac{\sigma_x}{2}\sin(\omega_j t + \varphi_j)\right], \quad (69)$$

with the initial condition $\rho_1^{(j)} = 0$. The resulting $\rho_1^{(j)}$ clearly also provide a solution for Eq. (67). Moreover, by rewriting Eq. (67) in the form

$$\frac{1}{\Omega_0}\frac{d\rho_1}{dt} = i\left[\rho_1, \frac{\sigma_z}{2}\right] + i\left[\rho_0, \frac{\sigma_x}{2}\left\{\sum_{j=1}^{\infty}\delta_j\sin(\omega_j t + \varphi_j)\right\}\right], \quad (70)$$

where we define $\rho_1 \equiv \sum_{j=1}^{\infty}\delta_j\rho_1^{(j)}$, and making use of the uniqueness theorem for differential equations, we note that the solution is unique.

In Eq. (68), we note the presence of mixed terms, involving parameters j and k. This is inconvenient; however, in the following derivations, we perform an average over the independent, fluctuating variables $\{\varphi_j, \varphi_k\} \in [0, 2\pi]$, which leads to a helpful simplification. Let us define the averaging procedure as

$$\langle f(\varphi)\rangle_\varphi = \frac{1}{2\pi}\int_0^{2\pi}f(\varphi)d\varphi. \quad (71)$$

In the derivations described below, it can be shown that

$$\left\langle\left[\rho_1^{(j)}, \frac{\sigma_x}{2}\sin(\omega_k t + \varphi_k)\right]\right\rangle_{\varphi_j,\varphi_k} =$$
$$\delta_{jk}\left\langle\left[\rho_1^{(j)}, \frac{\sigma_x}{2}\sin(\omega_j t + \varphi_j)\right]\right\rangle_{\varphi_j}, \quad (72)$$

where δ_{jk} is the Kronecker δ-function. As a result, we find that $\langle \rho_2^{(j,k)} \rangle_{\varphi_j, \varphi_k} = \delta_{jk} \langle \rho_2^{(j,j)} \rangle_{\varphi_j} \equiv \delta_{jk} \langle \rho_2^{(j)} \rangle_{\varphi_j}$. Anticipating this step, we can preemptively eliminate the mixed terms in Eq. (68), so that the sum runs only over the variable j. As was the case for $\rho_1^{(j)}$, we can then independently solve for each $\rho_2^{(j)}$, obtaining a unique solution for ρ_2. Equation (68) can therefore be replaced by the decoupled equation

$$\frac{1}{\Omega_0} \frac{d\rho_2^{(j)}}{dt} = i \left[\rho_2^{(j)}, \frac{\sigma_z}{2} \right] + i \left[\rho_1^{(j)}, \frac{\sigma_x}{2} \sin(\omega_j t + \varphi_j) \right]. \quad (73)$$

Thus, we may solve for the density matrix terms $\rho_1^{(j)}$ and $\rho_2^{(j)}$ independently, and combine the results for different j values afterwards.

Following the procedure described above, we perturbatively solve for ρ, apply initial conditions, and perform an average over the fluctuating variable φ_j, obtaining

$$\langle \rho(t) \rangle \approx \frac{1}{2} + \left[\frac{1}{2} \cos(\Omega_0 t) - \sum_{j=1}^{\infty} \delta_j^2 \frac{2\cos(\Omega_0 t) - 2\cos(\omega_j t) + (\Omega_0^2 - \omega_j^2)(t/\Omega_0)\sin(\Omega_0 t)}{8(\Omega_0^2 - \omega_j^2)^2/\Omega_0^4} \right] \sigma_x$$

$$+ \left[\frac{1}{2} \sin(\Omega_0 t) - \sum_{j=1}^{\infty} \delta_j^2 \frac{2\sin(\Omega_0 t) - 2(\omega_j/\Omega_0)\sin(\omega_j t) + (\Omega_0^2 - \omega_j^2)(t/\Omega_0)\cos(\Omega_0 t)}{8(\Omega_0^2 - \omega_j^2)^2/\Omega_0^4} \right] \sigma_y. \quad (74)$$

The perturbative expansion leading up to this result is formally related to a cumulant expansion [31], with an explicit, generalized averaging procedure.

Finally we note that certain terms in the σ_y sum of Eq. (74) diverge when $\omega_j \to \Omega_0$. However, we emphasize that the continuum limit is implied for both of the sums in Eq. (74), as discussed below. In this limit, the singularity is found to be integrable, provided that $S_{\delta\nu}(f)$ is smooth at $2\pi f = \Omega_0$, as discussed in Appendix . The singularity therefore poses no problem.

C. One-Photon Gate Fidelity

We now use Eq. (74) to compute quantum gate errors incurred during Rabi oscillations. In Appendix , we provide expressions that allow gate errors to be com-

puted numerically, for general gate periods, $t = t_g$. However analytical results are available for special gate periods. We specifically consider gates defined by the periods $t = 2\pi N/\Omega_0$ with $N = 1/2, 1, 3/2, \ldots$, where $N = 1/2$ corresponds to a π rotation, $N = 1$ corresponds to a 2π rotation, and so on. In the absence of fluctuations ($\delta_j = 0$), the ideal solution for such gates is given by

$$\rho_{\text{ideal}}(N) = \frac{1}{2} + \frac{1}{2}(-1)^{2N}\sigma_x. \quad (75)$$

Defining the gate errors as $\mathcal{E} = 1 - \mathcal{F}$, where $\mathcal{F} = \text{Tr}[\langle\rho\rangle\rho_{\text{ideal}}]$ is the gate fidelity, and making the substitutions $\omega_j \to 2\pi f$, $\Delta f \to df$, and

$$\sum_{j=1}^{\infty} \delta_j^2 \to \int_0^{\infty} \left(\frac{4\pi}{\Omega_0} \right)^2 S_{\delta\nu}(f) df, \quad (76)$$

we obtain

$$\mathcal{E} = 4\pi^2 \int_0^{\infty} S_{\delta\nu}(f) \frac{\Omega_0^2[1 - (-1)^{2N}\cos(4\pi^2 N f/\Omega_0)]}{(\Omega_0^2 - 4\pi^2 f^2)^2} df. \quad (77)$$

As noted above, this expression remains finite for all f, including $2\pi f = \Omega_0$. Repeating these calculations for the initial conditions $\rho(0) = \frac{1}{2}(1 + \sigma_y)$ and $\rho(0) = \frac{1}{2}(1 + \sigma_z)$, and performing an average over the results yields the average gate error [32]

$$\overline{\mathcal{E}} = \frac{8\pi^2}{3} \int_0^{\infty} S_{\delta\nu}(f) \frac{(\Omega_0^2 + 4\pi^2 f^2) \left[1 - (-1)^{2N}\cos(4\pi^2 N f/\Omega_0) \right]}{(\Omega_0^2 - 4\pi^2 f^2)^2} df. \quad (78)$$

ms text added In the remainder of the paper we will calculate $\mathcal{E}$ and $\overline{\mathcal{E}}$ in various scenarios. The error $\overline{\mathcal{E}}$ gives a state averaged error which is of interest for characterizing the typical performance of the gate operation. Alternatively $\mathcal{E}$ is the gate error for the particular case of the qubit starting in $|0\rangle$ in the computational basis, which is of particular relevance for optical excitation of Rydberg states.

Equation (78) is our main result, which may now be applied to cases of interest, including white noise and servo bumps. For the $t = 2\pi N/\Omega_0$ gates, defined above, with white noise defined in Eq. (32), we obtain the simple result

$$\mathcal{E} = \frac{\pi^3 h_0 N}{\Omega_0}, \quad \overline{\mathcal{E}} = \frac{4\pi^3 h_0 N}{3\Omega_0} \qquad \text{(white noise).} \quad (79)$$

It is worth noting here that implementing a π pulse ($N = 1/2$) starting in a computational basis state with error 10^{-4} at a Rabi rate of $\Omega_0/2\pi = 1$ MHz, with a laser that has a white noise spectrum, requires that $h_0 \leq 40$ Hz^2/Hz.

For servo bumps, the frequency noise is defined in Eq. (39). To simplify the error calculation, we make use of the fact that the peak in $S_{\delta\nu}(f)$ is typically sharper and narrower than other frequency-dependent terms in Eq. (78). This sharp peak can be observed, for example, in Fig. 3(c). We therefore make the following substitution in Eq (78):

$$S_{\delta\nu}(f) \rightarrow \frac{s_g f_g^2}{2}\delta(f - f_g), \quad (80)$$

which yields the following expressions for the gate error:

$$\mathcal{E} \approx 2 s_g (\pi f_g \Omega_0)^2 \frac{1 - (-1)^{2N}\cos(4\pi^2 N f_g/\Omega_0)}{(\Omega_0^2 - 4\pi^2 f_g^2)^2}$$
$$\text{(servo bump),} \quad (81)$$

$$\overline{\mathcal{E}} \approx \frac{4\pi^2 s_g f_g^2 (\Omega_0^2 + 4\pi^2 f_g^2)}{3(\Omega_0^2 - 4\pi^2 f_g^2)^2} \quad (82)$$
$$\times \left[1 - (-1)^{2N}\cos(4\pi^2 N f_g/\Omega_0)\right] \quad \text{(servo bump).}$$

As shown in later sections, the largest errors due to servo bumps occur when $\omega_g \approx 2\pi f_g = \Omega_0$. For integer or half-integer values of N, evaluating Eq. (83) in the limit $2\pi f_g \rightarrow \Omega_0$ (a worst-case scenario) gives

$$\mathcal{E} \approx \frac{s_g(\pi N)^2}{4}, \quad \overline{\mathcal{E}} \approx \frac{s_g(\pi N)^2}{3}. \quad (83)$$

Comparing Eqs. (79) and (83) we see that the worst-case error due to a servo bump is smaller than the error due to the background white noise when

$$s_g < \frac{4\pi h_0}{N\Omega_0}. \quad (84)$$

For the measured laser spectrum, shown in Fig. 3, the corresponding requirement for a π pulse with $\Omega_0/2\pi = 1$ MHz is $s_g < 1.0 \times 10^{-4}$. In this case, the measured s_g values for the two servo bumps ($s_{g1} = 1.3 \times 10^{-4}$ and $s_{g2} = 2.7 \times 10^{-4}$) do not satisfy this criterion. However, there is a known interplay between the stabilized white noise and the servo bumps [15]. From Eq. (83), we see that servo bumps are mainly dangerous when peaked at the Rabi frequency. When the servo bump peak is well separated from the Rabi frequency, the gate error is dominated by the white-noise background.
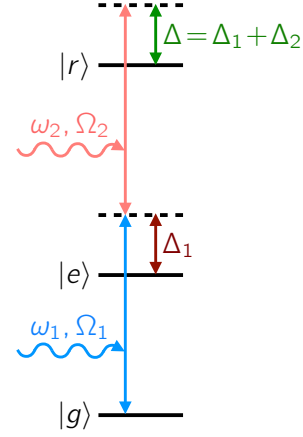

FIG. 4. Coupling scheme for two-photon Rabi oscillations in a ladder configuration, for states $|g\rangle$, $|e\rangle$, and $|r\rangle$. Two lasers are employed, with photon angular frequencies $\omega_{1,2}$, detunings $\Delta_{1,2}$, and associated Rabi angular frequencies $\Omega_{1,2}$. The lasers are detuned away from ladder excitations by angular frequencies Δ_1 and Δ_2.

D. Two-Photon Gate Fidelity

We can extend the time-series master equation approach to describe two-photon Rabi oscillations in the ladder geometry shown in Fig. 4. This approach is widely used for Rydberg excitation in quantum gate experiments with atomic qubits[33]. We consider a three-level system $\{|g\rangle, |e\rangle, |r\rangle\}$ with level energies given by E_g, E_e, and E_r. We also consider two monochromatic lasers with angular frequencies ω_1 and ω_2 and Rabi angular frequencies Ω_1 and Ω_2. As before, we allow for phase fluctuations in both lasers, characterized by their individual noise spectral densities, $S_{1,\delta\nu}(f)$ and $S_{2,\delta\nu}(f)$:

$$\phi_i(t) = -\sum_{j=1}^{N} \delta\nu_{i,j}\cos(2\pi f_j t + \varphi_{i,j}), \quad (85)$$

where

$$\delta\nu_{i,j} = -2\sqrt{S_{i,\delta\nu}(f_j)\Delta f}. \quad (86)$$

Here, the random phases $\{\varphi_{i,j}\}$ are assumed to be independent for all i and j.

In analogy with Eq. (59), the full system Hamiltonian in the laboratory frame is now given by

$$H = E_g|g\rangle\langle g| + E_e|e\rangle\langle e| + E_r|r\rangle\langle r|$$
$$+ \hbar\Omega_1\cos(\omega_1 t)\left(e^{-i\phi_1}|e\rangle\langle g| + e^{i\phi_1}|g\rangle\langle e|\right)$$
$$+ \hbar\Omega_2\cos(\omega_2 t)\left(e^{-i\phi_2}|r\rangle\langle e| + e^{i\phi_2}|e\rangle\langle r|\right) \quad (87)$$

Moving to the rotating frame defined by

$$U(t) = \exp\left[i\left(\frac{2\omega_1 t}{3} + \frac{\omega_2 t}{3}\right)(|e\rangle\langle e| - |g\rangle\langle g|)\right.$$
$$\left. +i\left(\frac{\omega_1 t}{3} + \frac{2\omega_2 t}{3}\right)(|r\rangle\langle r| - |e\rangle\langle e|)\right] \quad (88)$$

and applying an RWA, we obtain

$$H' \approx \frac{\hbar\Delta}{2}|g\rangle\langle g| - \frac{\hbar\delta}{2}|e\rangle\langle e| - \frac{\hbar\Delta}{2}|r\rangle\langle r|$$
$$+ \frac{\hbar\Omega_1}{2}\left(e^{-i\phi_1}|e\rangle\langle g| + e^{i\phi_1}|g\rangle\langle e|\right)$$
$$+ \frac{\hbar\Omega_2}{2}\left(e^{-i\phi_2}|r\rangle\langle e| + e^{i\phi_2}|e\rangle\langle r|\right), \quad (89)$$

where we have removed a constant energy term and defined $\hbar\Delta_1 = \hbar\omega_1 + E_g - E_e$, $\hbar\Delta_2 = \hbar\omega_2 + E_e - E_r$, $\Delta = \Delta_1 + \Delta_2$, as illustrated in Fig. 4, with $\delta = \Delta_1 - \Delta_2$.

As in the previous section, we next move to a fluctuation frame, defined by the transformation

$$U_\phi(t) = e^{-i\phi_1/2 - i\phi_2/2}|g\rangle\langle g|$$
$$+ e^{i\phi_1/2 - i\phi_2/2}|e\rangle\langle e| + e^{i\phi_1/2 + i\phi_2/2}|r\rangle\langle r|, \quad (90)$$

yielding the Hamiltonian

$$H'' \approx \frac{\hbar}{2}\left(\Delta + \dot{\phi}_1 + \dot{\phi}_2\right)|g\rangle\langle g|$$
$$+ \frac{\hbar}{2}\left(-\delta - \dot{\phi}_1 + \dot{\phi}_2\right)|e\rangle\langle e| + \frac{\hbar}{2}\left(-\Delta - \dot{\phi}_1 - \dot{\phi}_2\right)|r\rangle\langle r|$$
$$+ \frac{\hbar\Omega_1}{2}\left(|e\rangle\langle g| + |g\rangle\langle e|\right) + \frac{\hbar\Omega_2}{2}\left(|r\rangle\langle e| + |e\rangle\langle r|\right). \quad (91)$$

Now if we assume that $|\delta| \gg \Omega_1, \Omega_2, |\dot{\phi}_1|, |\dot{\phi}_2|$, and that the system wavefunction $|\psi\rangle$ is not initialized into state $|e\rangle$, then at later times we still have $|\langle\psi|e\rangle|^2 \ll 1$. Hence, it is a good approximation to slave $|e\rangle$ to states $|g\rangle$ and $|r\rangle$, such that

$$|e\rangle \approx \frac{\Omega_1}{\delta}|g\rangle + \frac{\Omega_2}{\delta}|r\rangle. \quad (92)$$

Eliminating $|e\rangle$ from H'', we arrive at an effective 2D Hamiltonian describing the dynamical evolution of $|g\rangle$ and $|r\rangle$:

$$H_{2D} \approx \frac{\hbar\tilde{\Omega}_0}{2}\sigma_x - \frac{\hbar}{2}\left(\Delta_+ + \dot{\phi}_1 + \dot{\phi}_2\right)\sigma_z, \quad (93)$$

where we define $\Delta_+ = \Delta + (\Omega_1^2 - \Omega_2^2)/2\delta$, $\tilde{\Omega}_0 = \Omega_1\Omega_2/\delta$, $\sigma_z = |r\rangle\langle r| - |g\rangle\langle g|$, and $\sigma_x = |r\rangle\langle g| + |g\rangle\langle r|$, and we have again removed a constant energy term. The shift Δ_+ is due to the dynamic Stark shift of the bare atomic levels that arises from the intermediate state detuning.

In the absence of noise ($\dot{\phi}_1, \dot{\phi}_2 = 0$), H_{2D} describes rotations tilted slightly away from the x axis, which is undesirable from a gating perspective. This situation can be avoided by adopting the special detuning value defined by the relation $\Delta_+ = 0$, or equivalently,

$$\Delta = \Delta_1\left(1 - \sqrt{1 + \frac{\Omega_1^2 - \Omega_2^2}{2\Delta_1^2}}\right). \quad (94)$$

For this case, we obtain

$$H_{2D} \approx \frac{\hbar\tilde{\Omega}_0}{2}\sigma_x - \frac{\hbar}{2}\left(\dot{\phi}_1 + \dot{\phi}_2\right)\sigma_z, \quad (95)$$

which maps immediately onto Eq. (61) of our previous one-photon analysis.

In the one-photon calculation, we were able to make progress by noting that the random phases φ_j, corresponding to frequency variables ω_j, were independent, yielding additive contributions to the total error in the quantum gates. Now in the two-photon case, the random variables φ_{j1} and φ_{j2}, corresponding to lasers 1 and 2, are also independent; therefore, their contributions to the total error should also be additive. Accounting for the separate power spectral densities in the two lasers, we obtain the following two-photon results, for gates defined by $t = 2\pi N/\tilde{\Omega}_0$, with $N = 1/2, 1, 3/2, \ldots$. For the white noise defined by the parameters h_1 and h_2 in the two lasers, and for the initial state $\rho(0) = \frac{1}{2}(1 + \sigma_x)$, we obtain

$$\mathcal{E} = \frac{\pi^3(h_1 + h_2)N}{\tilde{\Omega}_0} \quad \text{(white noise),} \quad (96)$$

which is relevant for Rydberg excitations. Averaging over initial states, we obtain the average gate fidelity

$$\overline{\mathcal{E}} = \frac{4\pi^3(h_1 + h_2)N}{3\tilde{\Omega}_0} \quad \text{(white noise).} \quad (97)$$

For the servo-bump model of laser phase noise, the differences in the lasers are characterized by the total power of the phase noise in the two servo bumps (s_{g1} and s_{g2}) and their corresponding peak frequencies (f_{g1} and f_{g2}). The resulting error for two-photon gates, for the initial state $\rho(0) = \frac{1}{2}(1 + \sigma_x)$, is given by

$$\mathcal{E} \approx 2s_{g1}(\pi f_{g1}\tilde{\Omega}_0)^2\frac{1 - (-1)^{2N}\cos(4\pi^2 N f_{g1}/\tilde{\Omega}_0)}{(\tilde{\Omega}_0^2 - 4\pi^2 f_{g1}^2)^2}$$
$$+ 2s_{g2}(\pi f_{g2}\tilde{\Omega}_0)^2\frac{1 - (-1)^{2N}\cos(4\pi^2 N f_{g2}/\tilde{\Omega}_0)}{(\tilde{\Omega}_0^2 - 4\pi^2 f_{g2}^2)^2}$$
$$\text{(servo bump).} \quad (98)$$

Averaging over initial states gives

$$\overline{\mathcal{E}} \approx \frac{4\pi^2 s_{g1} f_{g1}^2(\Omega_0^2 + 4\pi^2 f_{g1}^2)}{3(\Omega_0^2 - 4\pi^2 f_{g1}^2)^2} \quad (99)$$
$$\times \left[1 - (-1)^{2N}\cos(4\pi^2 N f_{g1}/\Omega_0)\right]$$
$$+ \frac{4\pi^2 s_{g2} f_{g2}^2(\Omega_0^2 + 4\pi^2 f_{g2}^2)}{3(\Omega_0^2 - 4\pi^2 f_{g2}^2)^2}$$
$$\times \left[1 - (-1)^{2N}\cos(4\pi^2 N f_{g2}/\Omega_0)\right] \quad \text{(servo bump).}$$

V. DYNAMICAL SIMULATION OF RABI OSCILLATIONS WITH PHASE NOISE

In this section, we perform simulations of Rabi oscillations, including laser phase fluctuations. We specifically consider the effects of white noise, defined in Eq. (32), for a range of noise amplitudes, $h_0 \in (0, 4000)$ Hz^2/Hz. We also consider servo bumps, defined in Eq. (39), for fixed parameter values of $h_g = 1100$ Hz^2/Hz and $\sigma_g = 1.4$ kHz, which are similar to the experimental values obtained in Sec. III. Since gate errors caused by servo bumps are maximized when the bump peak occurs near the Rabi frequency, $f_g \approx (\Omega_0/2\pi)$, we focus on the parameter range $f_g \in (0, 2) \times (\Omega_0/2\pi)$. In the latter simulations, we set the white-noise amplitude to $h_0 = 0$, to focus exclusively on the servo bump. For all simulations, we adopt the typical Rabi frequency $\Omega_0/2\pi = 1$ MHz. For the two-photon gates, for simplicity, we assume that both lasers have the same noise spectra.

A. One-photon gates

We first consider gates implemented with one-photon Rabi drives with laser phase noise. The gates are defined in Sec. IV C, with $N = 1/2$ (π rotations) and $N = 1$ (2π rotations). As previously, we assume that the qubit is driven resonantly. Defining $|\psi(t)\rangle = c_g(t)|g\rangle + c_e(t)|e\rangle$, the Schrödinger equation associated with Eq. (60) can be written as

$$\dot{c}_g = -i\frac{\Omega_0}{2}e^{-i\phi(t)}c_e, \qquad (100)$$

$$\dot{c}_e = -i\frac{\Omega_0}{2}e^{i\phi(t)}c_g. \qquad (101)$$

To solve these equations, we first obtain a random time trace for $\phi(t)$ from Eq. (56). The infinite series expansion must be truncated and we therefore write

$$\phi(t_k) = \sum_{j=1}^{M/2} 2\sqrt{S_\phi(f_j)\Delta f}\cos(2\pi f_j t_k + \varphi_j), \qquad (102)$$

where $\Delta f = f_{j+1} - f_j = 1/T$ for times sampled in the range $0 \leq t_k \leq T$, with $t_{k+1} - t_k = T/M$, according to the Nyquist sampling theorem. For the simulations described below, white noise poses the most serious challenge to numerical convergence. In this case, we find that a frequency bandwidth of $f_{M/2} = 10$ MHz is sufficient for our purposes, and that convergence is achieved when $M \approx 10^3$. Equations (100) and (101) are then solved numerically, using the computed time series. Statistical properties are obtained by performing averages over results from many random time series. As in previous sections, the resulting gate errors are defined as $1 - F$, where $F = \text{tr}[\langle\rho\rangle\rho_{\text{ideal}}]$.

In Fig. 5, we plot gate errors for π and 2π rotations in the presence of white noise. In this figure, as in all figures that follow, the numerical averages are shown as
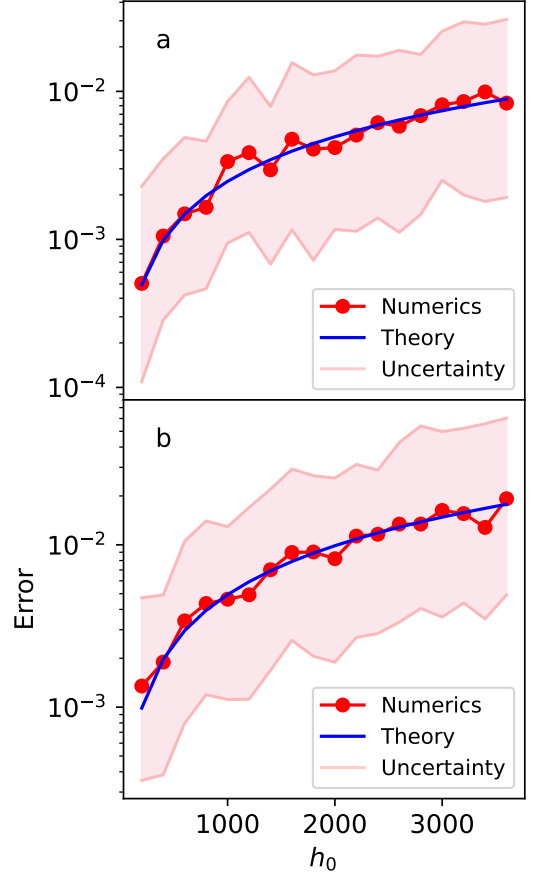

FIG. 5. Rabi errors for one-photon Rabi oscillations due to white phase noise, plotted as a function of noise amplitude h_0. Results are obtained following the procedure described in Sec. V A for (a) π rotations and (b) 2π rotations. Red markers represent averages from numerical simulations, while pink shading shows the corresponding 1σ error bars. Blue curves show theoretical results from Eq. (79).

red markers, while 1σ error bars are shown with pink shading. Theoretical results are shown as blue curves, obtained from Eq. (79). For typical white-noise amplitudes ($h_0 < 100$ Hz^2/Hz), the observed error levels are low. Theoretical results are found to reproduce the numerical ones quite accurately.

In Fig. 6, we plot π and 2π average gate errors for Rabi oscillations in the presence of servo-bump noise. Here the averages are performed over six initial states on the Bloch sphere ($\pm\hat{x}, \pm\hat{y}, \pm\hat{z}$) and results are plotted as a function of the center frequency of the servo bump, scaled by the Rabi frequency $\Omega_0/2\pi = 1$ MHz. The calculations are performed while holding the total power s_g and peak height h_g fixed at the values obtained for the larger servo bump in Fig. 3, while simultaneously varying the peak frequency f_g and width σ_g according to Eq. (41). Corresponding theory results are also shown, based on Eq. (83). Again, the theoretical results are found to describe well the non-monotonic behavior of the numerical
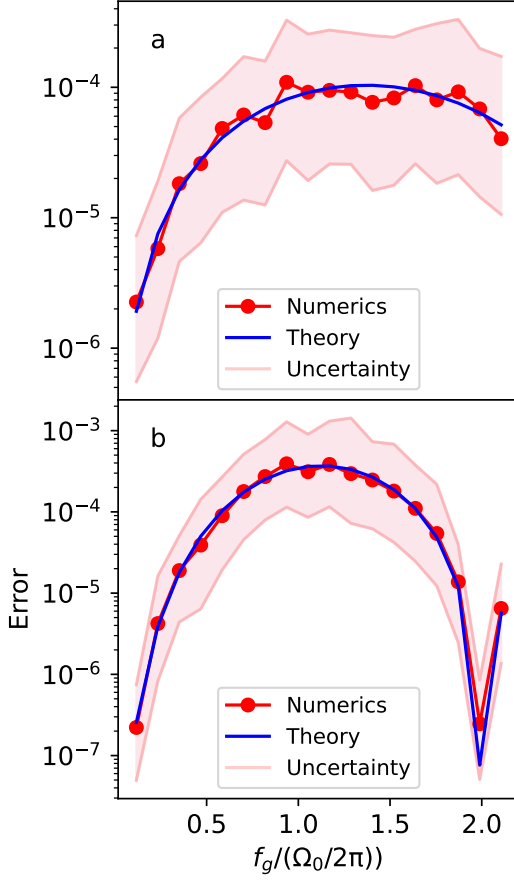
FIG. 6. Rabi errors for one-photon Rabi oscillations due to servo-bump phase noise. Results are plotted as a function of the center frequency of the servo bump f_g, scaled by the Rabi frequency $\Omega_0/2\pi = 1$ MHz, with additional noise parameters described in Sec. V A. Similar to Fig. 5, (a) shows results for π rotations and (b) shows results for 2π rotations. Theory results are obtained from Eq. (83).

results. As expected, gate errors are maximized for servo bumps centered near the Rabi frequency. As anticipated from the theoretical calculations of Sec. IV B, gate errors are strongly suppressed for the condition $f_g = 2(\Omega_0/2\pi)$. This is an interesting interference effect induced by the shape of Gaussian noise peaks, which isn't observed, for example, in the case of white noise. Such error suppression could potentially be leveraged for reducing Rabi gate errors.

In Fig. 7, we also show results for varying servo-bump noise levels. In this case, the center frequency of the servo bump is held fixed at the experimentally observed value $f_g = 234$ kHz reported in Sec. III, while the total noise power in the servo bump is varied, using the definition of s_g in Eq. (41).Plotted on a log-log scale, we observe an initial linear dependence of gate error on noise power.
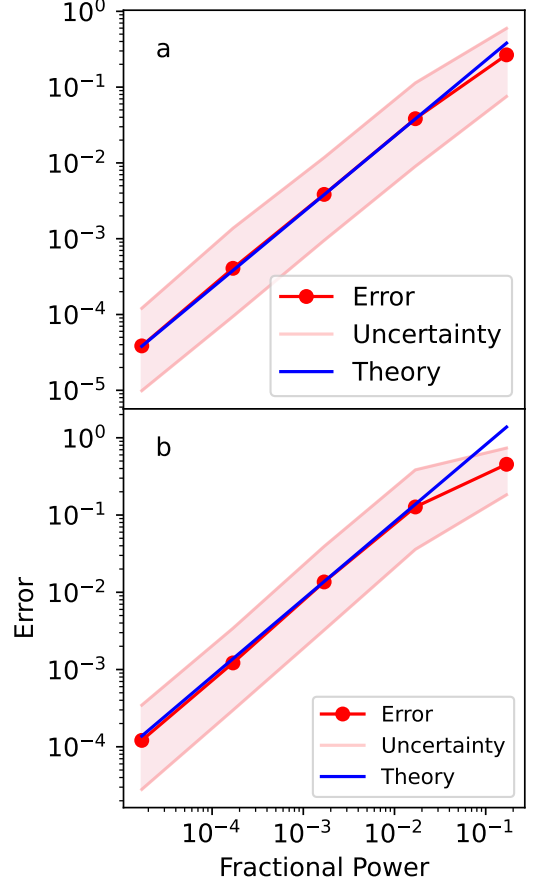

FIG. 7. Rabi errors for one-photon Rabi oscillations due to servo-bump phase noise: (a) π rotations, (b) 2π rotations. Calculations are very similar to Fig. 6, except that here, the central peak frequency of the servo bump is held fixed, while the total power s_g is varied, where s_g is defined in Eq. (41).

B. Two-photon gates

Two-photon gates are described in Sec. IV D. For the gates considered here, both lasers are detuned, in contrast with the one-photon gates described above. Defining $|\psi(t)\rangle = c_g(t)e^{-i\Delta t/2}|g\rangle + c_e(t)e^{i\delta t/2}|e\rangle + c_r(t)e^{i\Delta t/2}|r\rangle$, the Schrödinger equation associated with Eq. (89) can be written as

$$\dot{c}_g = -i\frac{\Omega_1}{2}e^{i\phi_1(t)}e^{i\Delta_1 t}c_e, \tag{103}$$

$$\dot{c}_e = -i\frac{\Omega_1}{2}e^{-i\phi_1(t)}e^{-i\Delta_1 t}c_g - i\frac{\Omega_2}{2}e^{i\phi_2(t)}e^{i\Delta_2 t}c_r, \tag{104}$$

$$\dot{c}_r = -i\frac{\Omega_2}{2}e^{-i\phi_2(t)}e^{-i\Delta_2 t}c_e. \tag{105}$$

As in experiments, the detuning parameters in two-photon simulations should be chosen carefully. Referring to the notation of Sec. IV D, we adopt the following criteria: (1) the effective, two-photon Rabi frequency is chosen to be $\tilde{\Omega}_0 = \Omega_1\Omega_2/\delta = 2\pi \times 1$ MHz (as in the
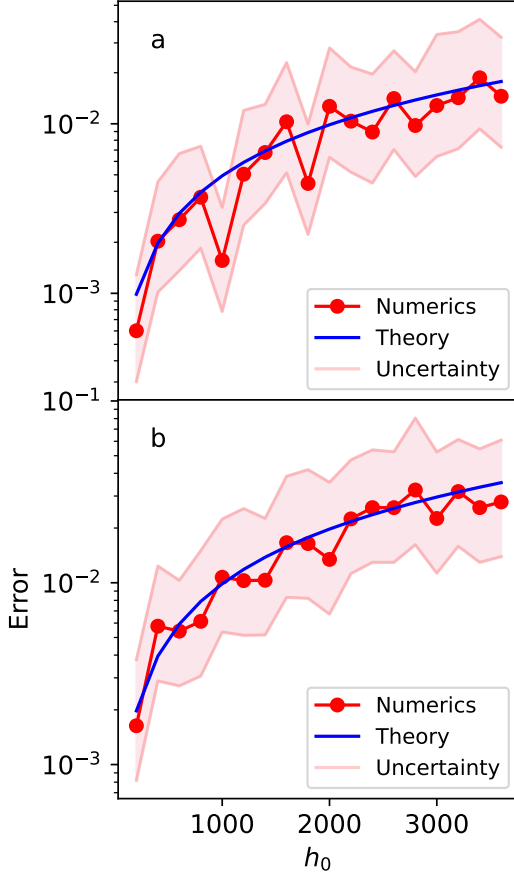
FIG. 8. Rabi errors for two-photon Rabi oscillations due to white phase noise: (a) π rotations, (b) 2π rotations. All simulations and plots are analogous to Fig. 5, while theory results are given by Eq. (97).

FIG. 9. Rabi errors for for two-photon Rabi oscillations due to servo-bump phase noise: (a) π rotations, (b) 2π rotations. All simulations and plots are analogous to Fig. 6, while theory results are given by Eq. (100).

one-photon simulations), (2) the ratio $\delta/\tilde{\Omega}_0$ should be large enough to avoid populating the intermediate level $|e\rangle$, but small enough for simulations to complete in a reasonable time (here we choose $\delta/\tilde{\Omega}_0 = 100$). Xiaoyu: this number is not consistent with other parameters used here. Please check. For convenience, we also choose $\Omega_1 = \Omega_2$, and we note that the resonance condition, Eq. (94), must be satisfied. These combined criteria yield $\Delta_1 = -\Delta_2 = 2\pi \times 5$ GHz, $\Omega_1 = \Omega_2 = 2\pi \times 100$ MHz, and $\delta = 2\pi \times 10$ GHz. These choices yield a resonant excitation of the state $|r\rangle$ ($\Delta = 0$; see Fig. 4), consistent with the resonant excitation scheme for one-photon gates. For convenience, we assume identical noise parameters for the two lasers (e.g., $h_1 = h_2$, etc.), although the time series for $\phi_1(t)$ and $\phi_2(t)$ are still generated independently from Eq. (102). Finally, Eqs. (103)-(105) are solved numerically for many random time series, and averaged.

Figure 8 shows two-photon results for the case of white phase noise. The corresponding theoretical results are given in Eq. (97). These results may be compared directly to one-photon gates. Indeed, the two-photon gate
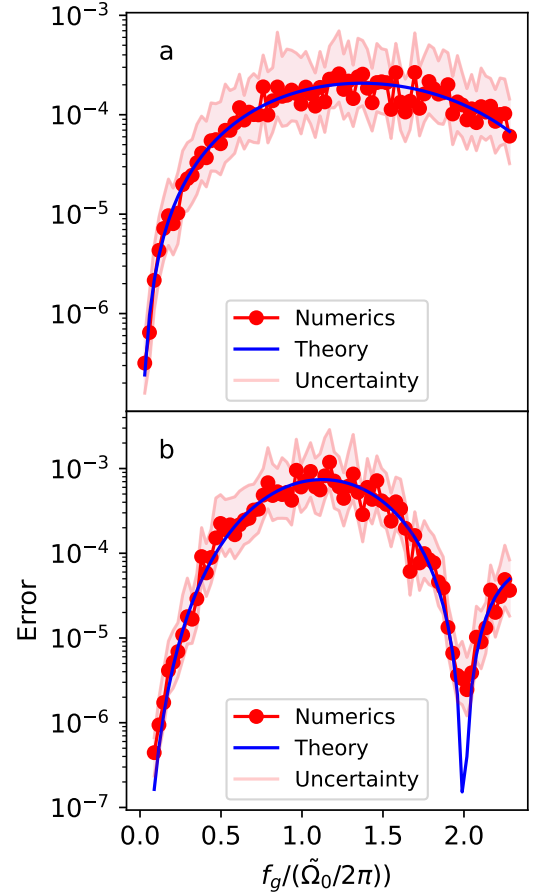
errors appear similar in shape, but doubled in magnitude, as compared to Fig. 5. This is consistent with the expectation that errors should be additive in the limit of weak noise, as confirmed in Sec. IV D.

Figure 9 shows two-photon results for the case of servo-bump phase noise. Here, the theoretical results are given in Eq. (100). Again, we observe an approximate doubling of the gates error as compared to the single-photon case, shown in Fig 6. In all cases, the theoretical results of Sec. IV appear quite accurate.

VI. BANDWIDTH-LIMITED PHASE NOISE AND THE QUASISTATIC LIMIT

Narrow bandwidth noise may provide a good approximation for certain highly filtered lasers. In this section, we extend the previous theoretical approach to the case of quasistatic phase noise, where the spectral content of the noise is restricted to very low frequencies. To begin, we consider the more general situation of bandwidth-limited

white noise, defined as

$$S_{\delta\nu}(f) = \begin{cases} h_0 & \text{when} & |f| \leq f_c, \\ 0 & \text{when} & |f| > f_c. \end{cases} \quad (106)$$

A noise spectrum of this type could describe a strongly filtered laser with no noise except a broadened carrier signal.

Di Domenico et al. [18] have studied how band-limited white noise is manifested in laser field noise, $S_E(f)$. They observe two distinct behaviors, with an abrupt transition between them occurring at $f_c = \pi^2 h_0/8\ln(2) \approx 1.78 h_0$. When $f_c \gtrsim 1.78 h_0$, $S_E(f)$ takes the form appropriate for white noise, which we previously characterized in Sec. II C. When $f_c \lesssim 1.78 h_0$, Eqs. (13) and (27) are readily solved, yielding

$$S_E(f) \approx \frac{|E_0|^2}{\sqrt{16\pi h_0 f_c}} e^{-f^2/4h_0 f_c}, \quad (107)$$

$$S_i(f) \approx \sqrt{\frac{3}{16\pi^3 h_0 t_d^2 f_c^3}} e^{-3f^2/16\pi^2 h_0 t_d^2 f_c^3}. \quad (108)$$

In the context of Rabi gate operations, when we also have $f_c \ll \Omega_0/2\pi$, we refer to this compressed-noise regime as quasistatic.

The singular nature of quasistatic noise causes the interrelations between $S_\phi(f)$, $S_E(f)$, and $S_i(f)$, embodied in Eqs. ((28) and (29), to collapse. This is particularly evident in Eq. (108) which does not exhibit the scallop features, typical of self-heterodyne measurements. We also note that the FWHM of the broadened carrier signals in Eqs. (107) and (108) are no longer related and exhibit distinct scaling properties. Hence, $S_i(f)$ may no longer be taken as a proxy for $S_E(f)$.

A. Master Equation Approach

While $S_{\delta\nu}(f)$, $S_E(f)$, and $S_i(f)$ depend only on h_0 and f_c, Rabi gate errors also depend on Ω_0. Single-photon gate errors caused by finite-bandwidth white noise can be computed from Eq. (78), without approximation, giving

$$\mathcal{E} = \frac{\pi h_0}{2\Omega_0} \left\{ \frac{2y[1 - (-1)^{2N}\cos(2\pi Ny)]}{1 - y^2} \right.$$
$$+ 2\text{Arctanh}(y) + \text{Ci}[2\pi N(1 - y)] - \text{Ci}[2\pi N(1 + y)]$$
$$\left. - 2\pi N\,\text{Si}[2\pi N(1 - y)] + 2\pi N\,\text{Si}[2\pi N(1 + y)] \right\},$$
$$(109a)$$

$$\overline{\mathcal{E}} = \frac{4\pi h_0}{3\Omega_0} \left\{ \frac{y[1 - (-1)^{2N}\cos(2\pi Ny)]}{1 - y^2} \right.$$
$$\left. - \pi N\,\text{Si}[2\pi N(1 - y)] + \pi N\,\text{Si}[2\pi N(1 + y)] \right\}, \quad (109b)$$

where $\text{Ci}(x)$ and $\text{Si}(x)$ are cosine and sine integral functions [34], and $y \equiv 2\pi f_c/\Omega_0$.

In the limit $f_c \gg \Omega_0$, Eqs. (109) reduce to the previously obtained results, Eqs. (79) and (97), for wide-bandwidth white noise. In the opposite limit, $f_c \lesssim \Omega_0$, we obtain the following results for $2\pi N$ Rabi gates:

$$\mathcal{E} \approx \begin{cases} \frac{8\pi^2 h_0 f_c}{\Omega_0^2} & (N = 1/2, 3/2, \dots), \\ \frac{32\pi^6 h_0 f_c^3 N^2}{3\Omega_0^4} & (N = 1, 2, \dots), \end{cases} \quad (110a)$$

$$\overline{\mathcal{E}} \approx \begin{cases} \frac{16\pi^2 h_0 f_c}{3\Omega_0^2} & (N = 1/2, 3/2, \dots), \\ \frac{64\pi^6 h_0 f_c^3 N^2}{9\Omega_0^4} & (N = 1, 2, \dots), \end{cases} \quad (110b)$$

where we have also taken $h_0 \lesssim \Omega_0$, as consistent with the weak-noise approximation. In this regime, we note that the results do not depend on f_c being larger or smaller than h_0. As in Sec. IV D, the two-photon gate errors are additive, yielding

$$\mathcal{E} = \begin{cases} \frac{8\pi^2(h_1 f_{c1} + h_2 f_{c2})}{\bar{\Omega}_0^2} & (N = 1/2, 3/2, \dots), \\ \frac{32\pi^6(h_1 f_{c1}^3 + h_2 f_{c2}^3)N^2}{3\bar{\Omega}_0^4} & (N = 1, 2, \dots), \end{cases} \quad (111a)$$

$$\overline{\mathcal{E}} = \begin{cases} \frac{16\pi^2(h_1 f_{c1} + h_2 f_{c2})}{3\bar{\Omega}_0^2} & (N = 1/2, 3/2, \dots), \\ \frac{64\pi^6(h_1 f_{c1}^3 + h_2 f_{c2}^3)N^2}{9\bar{\Omega}_0^4} & (N = 1, 2, \dots). \end{cases} \quad (111b)$$

Qualitatively different types of behavior are observed in Eqs. (110) and (111) for half vs. full rotations, which may be understood as follows. Frequency noise causes the Rabi rotation axis to tilt away from the equator of the Bloch sphere, resulting in gate errors. However, for the special case of full rotations, the Bloch state returns to its initial value (to leading order in a noise expansion), regardless of the tilted rotation axis. A secondary effect of the tilt is to increase the rotation speed, resulting in over-rotation. This effect is higher-order, however, yielding smaller errors for full rotations. In other words, for the special case of full rotations, in the limit of quasistatic noise, the leading-order contribution to the gate error vanishes; for all other cases, lower-order contributions are still present.

In Fig. 10, we show results of numerical simulations for bandwidth-limited white noise, for both π and 2π rotations. The corresponding theoretical predictions from Eq. (109) are also shown as blue curves. The theory clearly captures the majority of the errors arising from such noise spectra. However, for the case of 2π rotations, the theory breaks down in the limit of small f_c/h_0. Specifically, we find that Eq. (109) fails when $f_c \lesssim 1.43 h_0$. (Failure also requires that $f_c \lesssim \Omega_0/2\pi$.) We attribute this failure to the fact that the master equation derivation in Sec. IV employs an expansion in powers of the noise strength, keeping only the leading-order term. Hence, for the special case of full rotations, in the quasistatic limit (where the leading-order contribution to the gate error vanishes), our theory does not capture the central physics.
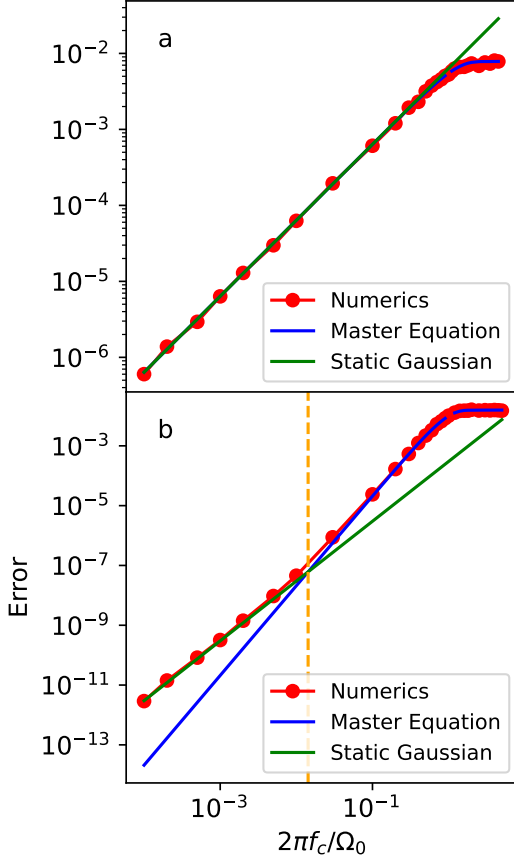
FIG. 10. One-photon Rabi errors for white, band-limited frequency noise with fixed amplitude $h_0 = 3.18$ kHz^2/kHz, as a function of the noise bandwidth, f_c. (a) π rotations. (b) 2π rotations. Here, red data correspond to numerical simulations, while the blue curves correspond to master-equation theory, Eq. (109), and the green curves correspond to quasistatic theory, Eq. (117). The master-equation result fails only for the special case of 2π rotations, for bandwidths below the (vertical-dashed) crossover frequency, $f_c \approx 1.43 h_0$. The quasistatic theory works well for both π and 2π rotations, for the case of narrow bandwidths.

B. Quasistatic Gaussian-Distributed Noise

To obtain an accurate solution for the singular problem of full rotations in the quasistatic limit, we modify the Master equation approach of Sec. IV B. The starting point for these calculations is the fluctuating frame Hamiltonian of Eq. (62),

$$H = \frac{\hbar\Omega_0}{2}\sigma_z + \frac{h\delta\nu}{2}\sigma_x, \qquad (112)$$

which describes a rotation tilted slightly away from the desired Rabi rotation axis. In the quasistatic limit, the frequency fluctuation $\delta\nu$ remains constant for the duration of the gate operation.

The dynamics of the density matrix is readily solved

for a static Hamiltonian, yielding

$$\rho(t) = \frac{1}{2} + \left\{ \frac{(2\pi\delta\nu)^2}{2\Omega_0'^2} + \frac{\Omega_0^2}{2\Omega_0'^2}\cos(\Omega_0't) \right\}\sigma_x$$
$$+ \left\{ \frac{\Omega_0}{2\Omega_0'}\sin(\Omega_0't) \right\}\sigma_y$$
$$+ \left\{ \frac{2\pi\delta\nu\,\Omega_0}{2\Omega_0'^2}[1 - \cos(\Omega_0't)] \right\}\sigma_z, \quad (113)$$

where $\Omega_0' \equiv \sqrt{\Omega_0^2 + (2\pi\delta\nu)^2}$, and we have adopted the same initial conditions as in Sec. IV B, namely, $\rho(0) = \frac{1}{2}(1 + \sigma_x)$.

Equation (113) describes the evolution of a pure state in a rotating frame. We now assume the fluctuation $\delta\nu$ is drawn from a Gaussian distribution with probability

$$p_{\delta\nu} = \frac{1}{\sigma_{\delta\nu}\sqrt{2\pi}}e^{-(\delta\nu)^2/2\sigma_{\delta\nu}^2}. \qquad (114)$$

Here, the connection to the bandwidth-limited white-noise power spectrum in Eq. (106) is provided through the variance:

$$\sigma_{\delta\nu}^2 = \langle(\delta\nu)^2\rangle_{\delta\nu} = \int_{-\infty}^{\infty} S_{\delta\nu}(f)df = 2h_0 f_c. \qquad (115)$$

As in Sec. IV C, the error in a Rabi gate defined by the gate period $t = 2\pi N/\Omega_0$ is given by error $= 1 - \text{tr}[\langle\rho\rangle_{\delta\nu}\rho_{\text{ideal}}]$, where ρ_{ideal} is defined in Eq. (75). Expanding Eq. (113) in leading powers of $2\pi\delta\nu/\Omega_0$, we obtain the following result for one-photon quasistatic gate errors:

$$\mathcal{E} \approx \begin{cases} \dfrac{8\pi^2 h_0 f_c}{\Omega_0^2} & (N = 1/2, 3/2, \dots), \\ \dfrac{48\pi^6 h_0^2 f_c^2 N^2}{\Omega_0^4} & (N = 1, 2, \dots). \end{cases} \qquad (116)$$

Repeating these calculations for the initial states $\rho(0) = \frac{1}{2}(1+\sigma_y)$ and $\rho(0) = \frac{1}{2}(1+\sigma_z)$, and averaging the results, gives the average gate error

$$\overline{\mathcal{E}} \approx \begin{cases} \dfrac{16\pi^2 h_0 f_c}{3\Omega_0^2} & (N = 1/2, 3/2, \dots), \\ \dfrac{32\pi^6 h_0^2 f_c^2 N^2}{\Omega_0^4} & (N = 1, 2, \dots). \end{cases} \qquad (117)$$

For the case of half-rotations ($N = 1/2, 3/2, \dots$), we note that Eq. (117) agrees with Eq. (110). However, for full rotations ($N = 1, 2, \dots$), the results disagree. We plot Eq. (117) as a green line in Fig. 10, finding that the quasistatic theory accurately captures the physics of both π and 2π rotations, for narrow bandwidths.

For two-photon gates, we follow a similar procedure. The Hamiltonian in the fluctuating frame, Eq. (95), can be rewritten as

$$H = \frac{\hbar\tilde{\Omega}_0}{2}\sigma_z + \frac{h(\delta\nu_1 + \delta\nu_2)}{2}\sigma_x, \qquad (118)$$

where $\delta\nu_1$ and $\delta\nu_2$ are the fluctuations of the two different lasers. After making the replacements $\Omega_0 \to \tilde{\Omega}_0 = \Omega_1\Omega_2/\delta$ and $\delta\nu \to \delta\nu_1 + \delta\nu_2$, the problem is then identical to Eq. (112). We note that, although $\tilde{\Omega}_0$ depends on the Rabi frequencies of the two lasers, the fluctuations are contained in parameters $\delta\nu_1$ and $\delta\nu_2$, not $\tilde{\Omega}_0$. Assuming independent Gaussian distributions for $\delta\nu_1$ and $\delta\nu_2$, as defined by their variances, $\sigma_{\delta\nu_1}^2 = 2h_1f_{c1}$ and $\sigma_{\delta\nu_2}^2 = 2h_2f_{c2}$, the error calculation then gives

$$\mathcal{E} \approx \begin{cases} \frac{8\pi^2(h_1f_{c1}+h_2f_{c2})}{\tilde{\Omega}_0^2} & (N = 1/2, 3/2, \dots), \\ \frac{48\pi^6(h_1f_{c1}+h_2f_{c2})^2N^2}{\tilde{\Omega}_0^4} & (N = 1, 2, \dots), \end{cases} \quad (119)$$

for the initial condition $\rho(0) = \frac{1}{2}(1 + \sigma_x)$, and

$$\overline{\mathcal{E}} \approx \begin{cases} \frac{16\pi^2(h_1f_{c1}+h_2f_{c2})}{3\tilde{\Omega}_0^2} & (N = 1/2, 3/2, \dots), \\ \frac{32\pi^6(h_1f_{c1}+h_2f_{c2})^2N^2}{\tilde{\Omega}_0^4} & (N = 1, 2, \dots) \end{cases} \quad (120)$$

for the average gate fidelity.

VII.   INTENSITY NOISE

Up to this point, we have only considered phase fluctuations of the laser field. We now also consider fluctuations of the field amplitude, or more specifically, the intensity $I(t)$, which is proportional to the laser power, or $|E_0|^2$. We define the fluctuating intensity as

$$I(t) = I_0 + \delta I(t) = I_0[1 + \alpha_I(t)] \quad (121)$$

where I_0 is the intensity of the noise-free laser and $\alpha_I(t)$ is the time-varying relative intensity fluctuation. The relative intensity noise (RIN) is a quantity frequently used to characterize the laser quality, defined as [21]

$$\text{RIN} = S_{\delta I}(f)/I_0^2 = S_{\alpha_I}(f), \quad (122)$$

where $S_{\delta I}(f)$ and $S_{\alpha_I}(f)$ are power spectral densities corresponding to the autocorrelation functions for δI and α_I, as defined in Eq. (4).

In certain types of lasers, including semiconductor diode lasers, relaxation oscillations may lead to intensity noise at frequencies of several GHz [35]. In principle, the effect of such wide-band intensity noise on gate fidelities can be calculated for arbitrary $S_{\alpha_I}(f)$, using methods similar to those derived in previous sections for phase noise. However, for optically pumped solid-state lasers, relaxation oscillations tend to be limited to much lower, sub-MHz frequencies[36]. These fluctuations are typically well below the Rabi frequency, and can therefore be considered as quasistatic for our purposes. The measured RIN of a solid-state Ti:Sa laser is shown in Fig. 11. Apart from narrow spikes at multiples of the 60 Hz power line frequency, the noise decreases rapidly with frequency such that the variance $\sigma_{\alpha_I}^2$ is primarily
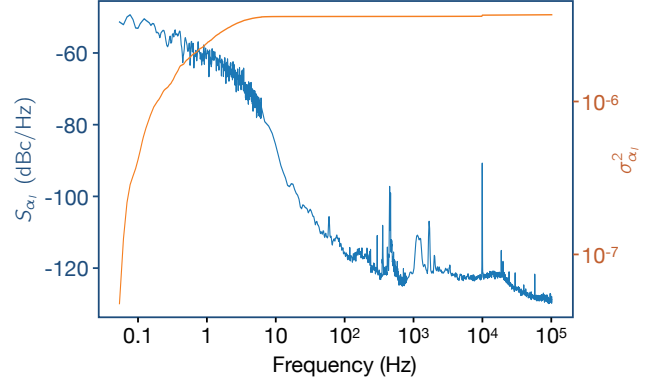

FIG. 11. Measured RIN spectrum of the Ti:Sa laser used in Fig. 3. The orange curve shows the integrated variance at frequency f, and indicates that nearly all intensity noise occurs below 10 Hz, so the quasistatic approximation should be excellent for this laser. The variance integrated from 0.1 - 10^5 Hz is $\sigma_{\alpha_I}^2 = 3.7 \times 10^{-6}$.
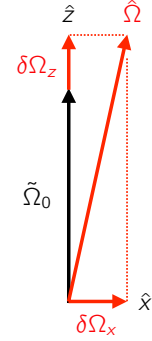

FIG. 12. Tilted rotation axis ($\hat{\Omega}$) for two-photon Rabi gates, due to intensity fluctuations.

due to frequencies below 10 Hz. We therefore expect a quasistatic analysis, as provided below, to be accurate.

Similar to the approach in the previous section, we assume the fluctuations of α_I are drawn from a Gaussian distribution with probability

$$p_{\alpha_I} = \frac{1}{\sigma_{\alpha_I}\sqrt{2\pi}}e^{-\alpha_I^2/2\sigma_{\alpha_I}^2}. \quad (123)$$

The connection to conventional RIN measurements is made through the variance:

$$\sigma_{\alpha_I}^2 = \langle\alpha_I^2\rangle_{\alpha_I} = \int_{-\infty}^{\infty} S_{\alpha_I}(f)df. \quad (124)$$

The time-varying Rabi frequency due to intensity noise, for one-photon gate operations, is given by $\Omega(t) = \Omega_0\sqrt{1 + \alpha_I(t)}$, where Ω_0 is the noise-free Rabi frequency. However, to avoid unphysical behavior in this expression, for the extremely unlikely event that $\alpha_I < -1$, we simply assume that $|\alpha_I| \ll 1$, to obtain the leading order

expression for the fluctuating Hamiltonian in the rotating frame, given by

$$H \approx \frac{\hbar \Omega_0}{2} \left(1 + \frac{\alpha_I}{2} \right) \sigma_z. \tag{125}$$

In this section we consider only the worst-case scenario for intensity-induced errors, which corresponds to the initial condition $\rho(0) = \frac{1}{2}(1 + \sigma_x)$, on the equator of the Bloch sphere in the fluctuating frame, and the north pole of the Bloch sphere in the laboratory frame of Eq. (59). Solving Eq. (63) for a given, time-independent fluctuation α_I, we then obtain

$$\rho(t) = \frac{1}{2} + \frac{1}{2} \cos \left[\Omega_0 \left(1 + \frac{\alpha_I}{2} \right) t \right] \sigma_x$$
$$+ \frac{1}{2} \sin \left[\Omega_0 \left(1 + \frac{\alpha_I}{2} \right) t \right] \sigma_y. \tag{126}$$

We again compute the error $\mathcal{E}$ for a Rabi gate defined by gate period $t = 2\pi N / \Omega_0$, where $\mathcal{E} = 1 - \text{tr}[\langle \rho \rangle_{\alpha_I} \rho_{\text{ideal}}]$ and ρ_{ideal} is defined in Eq. (75), obtaining

$$\mathcal{E} \approx \left\langle \frac{(\pi N \alpha_I)^2}{4} \right\rangle_{\alpha_I} = \frac{\pi^2 N^2 \sigma_{\alpha_I}^2}{4}. \tag{127}$$

For two-photon gates, the situation is only a little more complicated. Following the approach leading up to Eq. (95), and performing an additional rotation around the y axis, we obtain the approximate two-photon Rabi Hamiltonian,

$$H = \frac{\hbar \tilde{\Omega}}{2} \sigma_z + \frac{\hbar \Delta_+}{2} \sigma_x, \tag{128}$$

where we now include intensity noise:

$$\tilde{\Omega} = \frac{[\Omega_1(1 + \alpha_{I1}/2)][\Omega_2(1 + \alpha_{I2}/2)]}{\delta}$$
$$\approx \tilde{\Omega}_0 \left(1 + \frac{\alpha_{I1}}{2} + \frac{\alpha_{I2}}{2} \right), \tag{129}$$

Here, $\tilde{\Omega}_0$ is the noise-free version of the two-photon Rabi frequency. Including intensity noise, the effective detuning is given by

$$\Delta_+ = \Delta + \frac{\Omega_1^2(1 + \alpha_{I1}/2)^2 - \Omega_2^2(1 + \alpha_{I2}/2)^2}{2\delta}$$
$$\approx \Delta_{+,0} + \frac{\Omega_1^2 \alpha_{I1} - \Omega_2^2 \alpha_{I2}}{2\delta}, \tag{130}$$

where $\Delta_{+,0}$ is the noise-free detuning, which we set to zero to achieve full-range x rotations, as described in Sec. IV D.

The complication for two-photon gates is pictured in Fig. 12. As consistent with Eq. (129), the driving strength along the original Rabi rotation axis is modified by $\delta \Omega_z = \tilde{\Omega}_0(\alpha_{I1} + \alpha_{I2})/2$. However, in addition, the rotation axis is tilted by the presence of $\delta \Omega_x = \Delta_+$, where
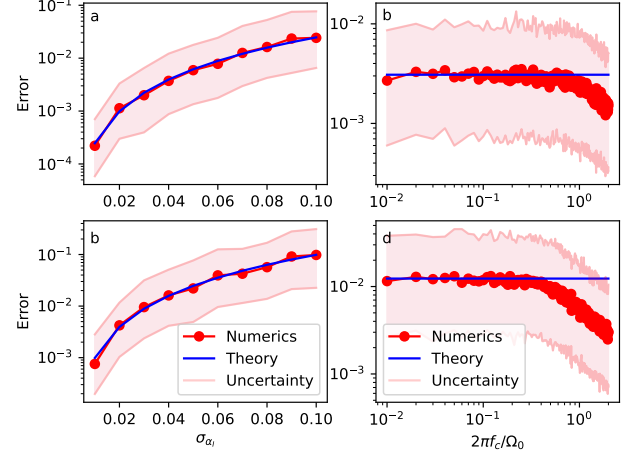

FIG. 13. Rabi errors due to RIN for one-photon gate operations. The first row, (a), (c), correspond to π-rotations, while the second row, (b), (d), correspond to 2π-rotations. The first column, (a), (b), corresponds to narrow-bandwidth noise, $f_c = 0.1 \times \Omega_0/2\pi$, while the second column, (c), (d), scan the cut-off frequency $f_c = 10 \times \Omega_0/2\pi$ with fixed σ_{α_I}=0.05. In all cases we choose $\Omega_0 = 2\pi \times 1$ MHz.

the average detuning $\overline{\Delta_+} = \Delta_{+,0} = 0$. The density matrix can be solved as before, to leading order in α_{I1} and α_{I2}, giving

$$\rho(t) = \frac{1}{2} + \frac{1}{2} \cos \left[\Omega_0 \left(1 + \frac{\alpha_{I1}}{2} + \frac{\alpha_{I2}}{2} \right) t \right] \sigma_x$$
$$+ \frac{1}{2} \sin \left[\Omega_0 \left(1 + \frac{\alpha_{I1}}{2} + \frac{\alpha_{I2}}{2} \right) t \right] \sigma_y + \rho_z \sigma_z, \tag{131}$$

where $\rho_z \propto \delta \Omega_x$. However, since ρ_{ideal} does not contain a σ_z component, ρ_z does not enter into the final error expression. The leading-order errors for two-photon gates are, therefore, found to be additive:

$$\mathcal{E} = \frac{\pi^2 N^2 (\sigma_{\alpha_{I1}}^2 + \sigma_{\alpha_{I2}}^2)}{4}. \tag{132}$$

To test these predictions, we simulate intensity noise by modeling it as finite-bandwidth white noise, using an approach very similar to Sec. VI B. Specifically, we define the intensity noise power spectral density as

$$S_{\alpha_I}(f) = \begin{cases} h_I & \text{when} & |f| \leq f_c, \\ 0 & \text{when} & |f| > f_c. \end{cases} \tag{133}$$

where f_c is the bandwidth. From Eq. (124), we see that $\sigma_{\alpha_I}^2 = 2 h_I f_c$, and since α_I is dimensionless, h_I must have units of time. In analogy with Eq. (102), we define

$$\alpha_I(t) = \sum_{j=1}^{M/2} 2 \sqrt{S_{\alpha_I}(f_j) \Delta f} \cos(2\pi f_j t + \varphi_j), \tag{134}$$

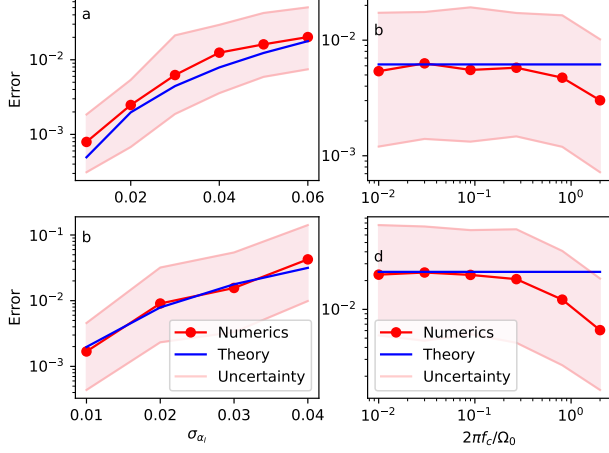where $\phi_j \in [0, 2\pi]$, as usual.

FIG. 14. Rabi errors due to RIN for two-photon gate operations. All panels and simulations parameters are the same as in Fig. 13, but with Ω_0 replaced by $\tilde{\Omega}_0$. **ms** Xiaoyu - please update so 2nd column scans f_x as in Fig. 13

We now solve Eqs. (100) and (101) numerically, using the one-photon Rabi frequency $\Omega(t) = \Omega_0 \sqrt{1 + \alpha_I(t)} \approx \Omega_0[1 + \alpha_I(t)/2]$ for a given time series $\alpha(t)$, generated from Eq. (134). The procedure is repeated for many random time series and the results are averaged to compute the fidelity F and the error $1 - F$.

The results of these numerical simulations are shown in Fig. 13 for π and 2π rotations, and for the cases of narrow-bandwidth noise $f_c \ll \Omega_0/2\pi$ and wide-bandwidth noise $f_c \gg \Omega_0/2\pi$. For a given plot, f_c is held fixed while σ_{α_I} is swept. Due to the constraints of our noise model, this implies that we sweep the parameter $h_I = \sigma_{\alpha_I}^2/2f_c$. In the figure, we see that the results are well described by our theoretical predictions in Eq. (127) for the low-bandwidth regime, as expected, but diverge quantitatively in the high-bandwidth regime.

For two-photon gates, we follow the same procedure, now using the two-qubit Rabi frequency of Eq. (129). The corresponding results are shown in Fig. 14. We again obtain good agreement with our theoretical predictions in Eq. (132) for the low-bandwidth regime, but poor agreement for the high-bandwidth regime.

VIII. SUMMARY AND DISCUSSION

In this paper, we theoretically investigated errors in quantum gate operations of neutral-atom qubits. We focused on a noise mechanism that dominates many qubit experiments: phase fluctuations of the driving laser. We considered both one and two-photon Rabi oscillations. We also considered generic noise spectra, such as flat-background (white) noise, and noise peaked at finite frequencies. We refer to the latter as 'servo-bump noise,'

due to the common occurrence of noise peaks due to servo-loop feedback circuitry.

We have specifically considered the weak-noise regime, which is typical of modern qubit experiments. In this limit, we uncover simple relations between the underlying phase-noise spectra and noise spectra measured in self-heterodyne experiments. These relations are given in Eqs. (14), (28), and (29), and they allow us to analyze and fit experimental self-heterodyne data using specific white and servo-bump noise models, as described in Sec. III.

The weak-noise limit also allows us to solve a master equation, describing the effects of laser phase noise on Rabi oscillations, which we then use to calculate gate fidelities. We perform realistic numerical simulations of Rabi gates by generating random time series that include white and servo-bump phase noise. The results are well explained by our master equation solutions, yielding a deeper understanding of the decoherence process. Our main results are given in Eqs. (78), (83), (97), and (100).

In the case of servo-bump phase noise, we observe that gate errors are most prominent when the central frequency of the noise peak occurs near the Rabi frequency, as expected for $T_{1\rho}$-type noise mechanisms [5]. For π pulses the gate-error peak frequency falls in the range $1 \leq f_g/(\Omega_0/2\pi) \leq 1.5$. The one-photon error contributions from white noise and servo bumps are given by Eqs. (79) and (83) respectively. For a two-photon drive the white noise and servo bump errors are given by Eqs. (97) and (100) respectively. For a 2π pulse the gate-error peak frequency is close to $f_g = \Omega_0/2\pi$. Away from these peaks, the gate error may be suppressed by many orders of magnitude, such that the residual errors are dominated by background noise (e.g., weak white noise). Generally, the contributions to the gate error from different noise mechanisms are found to be additive in the weak-noise regime.

ms add discussion of comparison with Biercuk

To demonstrate how these results may be used to guide future experiments, we consider the case of π-rotations ($N = 1/2$), starting in a computational basis state with two-photon driving. Assuming a Rabi frequency of $\tilde{\Omega}_0/2\pi = 1$ MHz the requirement on the white noise background to reach a gate error of 10^{-4} is $h_0 = 20$ Hz^2/Hz for each laser field. As shown in Fig. 3 a locked Ti:Sa laser satisfies this requirement, while other laser types such as semiconductor diode lasers typically have larger frequency noise, even if locked to a reference cavity[23].

If a servo bump is present and its peak frequency occurs near the Rabi frequency of one of the two transitions, then achieving a gate-error level of 10^{-4} would require a total (integrated) servo bump noise power of no more than $s_g = 0.00016$. (Note that s_g, as defined here, includes the power in the servo bumps on both sides of the carrier peak.) In the self-heterodyne noise measurements analyzed in Sec. III, we observed noise powers of $s_{g1} = 0.00013$ and $s_{g2} = 0.00027$. Moreover, since

the peak frequency of the larger servo bump occurs at $f_g = 234$ kHz, we can suppress its effect on the fidelity by choosing a Rabi frequency of $\Omega_0/2\pi \sim 117$ kHz, or alternatively, a Rabi frequency larger than 1 - 2 MHz. In this way, we can realistically expect to achieve gate errors below 10^{-4} in this system. For more complex gate operations, such as Rydberg gates for preparing entangled states, longer pulses are involved and the requirements on laser noise are correspondingly more stringent. A two-qubit entangling Rydberg gate requires about 2π of ground-Rydberg rotation on each atom. This implies that limiting the laser noise contribution to gate fidelity to below 10^{-4} requires a white noise spectrum with a more demanding noise level of $h_0 \lesssim 5$ Hz^2/Hz.

Similar estimates of the RIN level required for a desired gate fidelity can be easily made. Assuming the RIN is concentrated at frequencies much lower than the Rabi frequency Eq. (132) shows that the gate error is independent of Ω_0. For a two-photon π pulse with error at the 10^{-4} level the RIN variance must satisfy $\sigma^2 \lesssim 8. \times 10^{-5}$ and for a Rydberg entangling gate with error of 10^{-4} we need $\sigma^2 \lesssim 1. \times 10^{-5}$. The data in Fig. 11 show that this variance level is reached with a well stabilized laser, although the relevant variance is the light seen by the atomic qubit which typically has increased variance due to instability of optical components as well as atomic position fluctuations[37].

In the limit of weak noise the errors due to laser phase noise and RIN are additive. It is apparent that achieving very high fidelity optically driven gate operations puts stringent limits on laser noise parameters. This is true for one-photon and two-photon drives in the ladder configuration considered here. The highest fidelity optically driven gate we are aware of is the demonstration of Raman gates on trapped ^{9}Be$^+$ ions using a two-photon Λ configuration where an average error per gate of 3.8×10^{-5} was achieved[38]. Notably the use of a Λ configuration with both beams derived from the same laser implies a cancellation of phase noise that is not present in the ladder configuration analyzed here.

IX. ACKNOWLEDGEMENT

Appendix A: Fidelity measures

`ms` add text

Appendix B: Error estimates for arbitrary Rabi gates

In the main text, we computed errors for Rabi gates with gate periods $t = 2\pi N/\Omega_0$, for $N = 1/2, 1, 3/2, \dots$. These special gates were chosen because they can be solved analytically. However, the master equation formalism developed in this work can be applied to arbitrary Rabi gates.

Let us consider the arbitrary gate period $t = t_g$. Making the substitutions $\omega_j \to 2\pi f$, $\Delta f \to df$, as well as the substitution in Eq. (76), Eq. (74) can be rewritten as

$$
\begin{aligned}
\langle \rho(t_g) \rangle \approx \frac{1}{2} &+ \left[\frac{1}{2}\cos(\Omega_0 t_g) - 2\pi^2\Omega_0^2 \int_0^\infty df\, S_{\delta\nu}(f) \frac{2\cos(\Omega_0 t_g) - 2\cos(2\pi f t_g) + (\Omega_0^2 - 4\pi^2 f^2)(t_g/\Omega_0)\sin(\Omega_0 t_g)}{(\Omega_0^2 - 4\pi^2 f^2)^2} \right] \sigma_x \\
&+ \left[\frac{1}{2}\sin(\Omega_0 t_g) - 2\pi^2\Omega_0^2 \,\text{p.v.}\! \int_0^\infty df\, S_{\delta\nu}(f) \frac{2\sin(\Omega_0 t_g) - 2(2\pi f/\Omega_0)\sin(2\pi f t_g) + (\Omega_0^2 - 4\pi^2 f^2)(t_g/\Omega_0)\cos(\Omega_0 t_g)}{(\Omega_0^2 - 4\pi^2 f^2)^2} \right] \sigma_y,
\end{aligned}
\tag{B1}
$$

where p.v. stands for principal value (applied at the singularity, $f \to \Omega_0/2\pi$), and we have made use of the facts that (1) the singularity in the integrand takes the form $(\Omega_0 - 2\pi f)^{-1}$, and (2) $S_{\delta\nu}(f)$ is generally a smooth function near $f = \Omega_0/2\pi$. In this form, Eq. (B1) can be solved numerically.

We may also compute the gate error associated with Eq. (B1) by noting that

$$
\rho_{\text{ideal}}(t_g) = \frac{1}{2} + \frac{1}{2}\cos(\Omega_0 t_g)\sigma_x + \frac{1}{2}\sin(\Omega_0 t_g)\sigma_y.
\tag{B2}
$$

Defining the gate error as usual by $1 - F$, where $F = \text{Tr}[\langle\rho\rangle\rho_{\text{ideal}}]$, we obtain

$$
\begin{aligned}
\text{error} \approx\ &(2\pi\Omega_0)^2 \cos(\Omega_0 t_g) \int_0^\infty df\, S_{\delta\nu}(f) \frac{2\cos(\Omega_0 t_g) - 2\cos(2\pi f t_g) + (\Omega_0^2 - 4\pi^2 f^2)(t_g/\Omega_0)\sin(\Omega_0 t_g)}{(\Omega_0^2 - 4\pi^2 f^2)^2} \\
&+ (2\pi\Omega_0)^2 \sin(\Omega_0 t_g) \,\text{p.v.}\! \int_0^\infty df\, S_{\delta\nu}(f) \frac{2\sin(\Omega_0 t_g) - 2(2\pi f/\Omega_0)\sin(2\pi f t_g) + (\Omega_0^2 - 4\pi^2 f^2)(t_g/\Omega_0)\cos(\Omega_0 t_g)}{(\Omega_0^2 - 4\pi^2 f^2)^2},
\end{aligned}
\tag{B3}
$$

which can also be solved numerically.

[1] E. Geva, R. Kosloff, and J. L. Skinner, "On the relaxation of a two-level system driven by a strong electromagnetic field," J. Chem. Phys. **102**, 8541 (1995).

[2] Yu. Makhlin and A. Shnirman, "Dephasing of qubits by transverse low-frequency noise," JETP Lett. **8**, 497 (2003).

[3] G. Ithier, E. Collin, P. Joyez, P. J. Meeson, D. Vion, D. Esteve, F. Chiarello, A. Shnirman, Y. Makhlin, J. Schriefl, and G. Schön, "Decoherence in a superconducting quantum bit circuit," Phys. Rev. B **72**, 134519 (2005).

[4] Z. Chen, J. G. Bohnet, J. M. Weiner, and J. K. Thompson, "General formalism for evaluating the impact of phase noise on Bloch vector rotations," Phys. Rev. A **86**, 032313 (2012).

[5] F. Yan, S. Gustavsson, J. Bylander, X. Jin, F. Yoshihara, D. G. Cory, Y. Nakamura, T. P. Orlando, and W. D. Oliver, "Rotating-frame relaxation as a noise spectrum analyser of a superconducting qubit undergoing driven evolution," Nat. Commun. **4**, 2337 (2013).

[6] E. Paladino, Y. M. Galperin, G. Falci, and B. L. Altshuler, "$1/f$ noise: Implications for solid-state quantum information," Rev. Mod. Phys. **86**, 361 (2014).

[7] F. Yoshihara, Y. Nakamura, F. Yan, S. Gustavsson, J. Bylander, W. D. Oliver, and J.-S. Tsai, "Flux qubit noise spectroscopy using Rabi oscillations under strong driving conditions," Phys. Rev. B **89**, 020503 (2014).

[8] J. Jing, P. Huang, and X. Hu, "Decoherence of an electrically driven spin qubit," Phys. Rev. A **90**, 022118 (2014).

[9] T. Green, H. Uys, and M. J. Biercuk, "High-order noise filtering in nontrivial quantum logic gates," Phys. Rev. Lett. **109**, 020501 (2012).

[10] T. J. Green, J. Sastrawan, H. Uys, and M. J. Biercuk, "Arbitrary quantum control of qubits in the presence of universal noise," New J. Phys. **15**, 095004 (2013).

[11] A. Soare, H. Ball, D. Hayes, J. Sastrawan, M. C. Jarratt, J. J. McLoughlin, X. Zhen, T. J. Green, and M. J. Biercuk, "Experimental noise filtering by quantum control," Nat. Phys. **10**, 825 (2014).

[12] H. Ball, W. D. Oliver, and M. J. Biercuk, "The role of master clock stability in quantum information processing," npj Qu. Inf. **2**, 16033 (2016).

[13] S. de Léséleuc, D. Barredo, V. Lienhard, A. Browaeys, and T. Lahaye, "Analysis of imperfections in the coherent optical excitation of single atoms to Rydberg states," Phys. Rev. A **97**, 053803 (2018).

[14] M. Zhang, Y. Xie, J. Zhang, W. Wang, C. Wu, T. Chen, W. Wu, and P. Chen, "Estimation of the laser frequency noise spectrum by continuous dynamical decoupling," Phys. Rev. Appl. **15**, 014033 (2021).

[15] M. L. Day, P. J. Low, B. White, R. Islam, and C. Senko, "Limits on atomic qubit control from laser noise," npj Qu. Inf. **8**, 72 (2022).

[16] H. Levine, A. Keesling, A. Omran, H. Bernien, S. Schwartz, A. S. Zibrov, M. Endres, M. Greiner, V. Vuletić, and M. D. Lukin, "High-fidelity control and entanglement of Rydberg-atom qubits," Phys. Rev. Lett. **121**, 123603 (2018).

[17] T. Okoshi, K. Kikuchi, and A. Nakayama, "Novel method for high resolution measurement of laser output spectrum," El. Lett. **16**, 630 (1980).

[18] G. Di Domenico, S. Schilt, and P. Thomann, "Simple approach to the relation between laser frequency noise and laser line shape," Appl. Opt. **49**, 4801 (2010).

[19] D. S. Elliott, R. Roy, and S. J. Smith, "Extracavity laser band-shape and bandwidth modification," Phys. Rev. A **26**, 12 (1982).

[20] M. Zhu and J. L. Hall, "Stabilization of optical phase/frequency of a laser system: application to a commercial dye laser with an external stabilizer," J. Opt. Soc. Am. B **10**, 802 (1993).

[21] F. Riehle, *Frequency standards basics and applications* (Wiley-VCH, 2004).

[22] P. B. Gallion and G. Debarge, "Quantum phase noise and field correlation in single frequency semiconductor laser systems," IEEE J. Qu. Electr. **20**, 343 (1984).

[23] Y. Li, Z. Fu, L. Zhu, J. Fang, H. Zhu, J. Zhong, P. Xu, X. Chen, J. Wang, and M. Zhan, "Laser frequency noise measurement using an envelope-ratio method based on a delayed self-heterodyne interferometer," Opt. Commun. **435**, 244 (2019).

[24] H. Tsuchida, "Laser frequency modulation noise measurement by recirculating delayed self-heterodyne method," Opt. Lett. **36**, 681 (2011).

[25] L. Richter, H. Mandelberg, M. Kruger, and P. McGrath, "Linewidth determination from self-heterodyne measurements with subcoherence delay times," IEEE J. Qu. Electr. **22**, 2070 (1986).

[26] R. W. P. Drever, J. L. Hall, F. V. Kowalski, J. Hough, G. M. Ford, A. J. Munley, and H. Ward, "Laser phase and frequency stabilization using an optical resonator," Appl. Phys. B **31**, 97 (1983).

[27] T. M. Graham, Y. Song, J. Scott, C. Poole, L. Phuttitarn, K. Jooya, P. Eichler, X. Jiang, A. Marra, B. Grinkemeyer, M. Kwon, M. Ebert, J. Cherek, M. T. Lichtman, M. Gillette, J. Gilbert, D. Bowman, T. Ballance, C. Campbell, E. D. Dahl, O. Crawford, N. S. Blunt, B. Rogers, T. Noel, and M. Saffman, "Multi-qubit entanglement and algorithms on a neutral-atom quantum computer," Nature **604**, 457–462 (2022).

[28] M. J. Tucker, P. G. Challenor, and D. J. T. Carter, "Numerical simulation of a random sea: a common error and its effect upon wave group statistics," Appl. Ocean Res. **6**, 118 (1984).

[29] J.-B. Saulnier, P. Ricci, A. F. Falcao, and A. H. Clement, "Mean Power Output Estimation of WECs in Simulated Sea-States," in *8th European Wave & Tidal Energy Conference* (Uppsala, Sweden, 2009).

[30] Th. Haslwanter, H. Ritsch, J. Cooper, and P. Zoller, "Laser-noise-induced population fluctuations in two- and three-level systems," Phys. Rev. A **38**, 5652–5659 (1988).

[31] R. Kubo, "Stochastic Liouville equations," J. Math.

Phys. **4**, 174 (1963).

[32] M. A. Nielsen, "A simple formula for the average gate fidelity of a quantum dynamical operation," Phys. Lett. A **303**, 249 (2002).

[33] T. A. Johnson, E. Urban, T. Henage, L. Isenhower, D. D. Yavuz, T. G. Walker, and M. Saffman, "Rabi oscillations between ground and Rydberg states with dipole-dipole atomic interactions," Phys. Rev. Lett. **100**, 113003 (2008).

[34] The sine and cosine integral functions are defined as $\mathrm{Si}(z) = \int_0^z (\sin t)/t \, dt$ and $\mathrm{Ci}(z) = -\int_z^\infty (\cos t)/t \, dt$.

[35] K. Vahala, Ch. harder, and A. Yariv, "Observation of relaxation resonance effects in the field spectrum of semi-conductor lasers," Appl. Phys. lett. **42**, 211 (1983).

[36] W. Koechner, "Output fluctuations of CW-pumped Nd:YAG lasers," IEEE J. Qu. Electr. **8**, 656 (1972).

[37] K. Gillen-Christandl, G. Gillen, M. J. Piotrowicz, and M. Saffman, "Comparison of Gaussian and super Gaussian laser beams for addressing atomic qubits," Appl. Phys. B **122**, 131 (2016).

[38] J. P. Gaebler, T. R. Tan, Y. Lin, Y. Wan, R. Bowler, A. C. Keith, S. Glancy, K. Coakley, E. Knill, D. Leibfried, and D. J. Wineland, "High-fidelity universal gate set for $^9\mathrm{Be}^+$ ion qubits," Phys. Rev. Lett. **117**, 060505 (2016).